


Cite this: *RSC Adv.*, 2024, 14, 13258

# Bishydrazone ligand and its Zn-complex: synthesis, characterization and estimation of scalability inhibition mitigation effectiveness for API 5L X70 carbon steel in 3.5% NaCl solutions†

Ola. A. El-Gammal,<sup>a</sup> Dina A. Saad,<sup>a</sup> Marwa N. El-Nahass,<sup>b</sup> Kamal Shalabi<sup>ID</sup> \*<sup>c</sup> and Yasser M. Abdallah<sup>ID</sup> \*<sup>d</sup>

Bishydrazone ligand, 2,2'-thiobis(*N'*-(*E*-thiophen-2-ylmethylene) acetohydrazide), H<sub>2</sub>TTAH and its Zn-complex were prepared and characterized through elemental analysis and various spectroscopic performances as well as (IR, <sup>1</sup>H and <sup>13</sup>C NMR, mass and (UV-Vis) measurements. The synthesized complex exhibited the molecular formula [Zn<sub>2</sub>(H<sub>2</sub>TTAH)(OH)<sub>4</sub>(C<sub>5</sub>H<sub>5</sub>N)<sub>3</sub>C<sub>2</sub>H<sub>5</sub>OH] (Zn-H<sub>2</sub>TTAH). To assess their potential as anti-corrosion materials, the synthesized particles were assessed for their effectiveness for API 5L X70 C-steel corrosion in a 3.5% NaCl solution using electrochemical methods such as potentiodynamic polarization (PP) and electrochemical impedance spectroscopy (EIS). Additionally, X-ray photoelectron spectroscopy (XPS) was employed to examine the steel surface treated with the tested inhibitors, confirming the establishment of an adsorbed protecting layer. The results obtained from the PP plots indicated that both H<sub>2</sub>TTAH and Zn-H<sub>2</sub>TTAH act as mixed-type inhibitors. At a maximum concentration of 1 × 10<sup>-4</sup> M, H<sub>2</sub>TTAH and Zn-H<sub>2</sub>TTAH exhibited inhibition efficiencies of 93.4% and 96.1%, respectively. The adsorption of these inhibitors on the steel surface followed the Langmuir adsorption isotherm, and it was determined to be chemisorption. DFT calculations were achieved to regulate the electron donation ability of H<sub>2</sub>TTAH and Zn-H<sub>2</sub>TTAH molecules. Additionally, Monte Carlo (MC) simulations were conducted to validate the adsorption configurations on the steel surface and gain insight into the corrosion inhibition mechanism facilitated by these molecules.

Received 15th January 2024

Accepted 13th April 2024

DOI: 10.1039/d4ra00404c

rsc.li/rsc-advances

## 1. Introduction

Every year, corrosion causes significant global repercussions as metallic materials deteriorate due to various chemical, biological, and electrochemical processes when they interact with their environment.<sup>1</sup> Carbon steel is commonly utilized in manufacturing according to its superior mechanical properties, robust tensile strength, and cost-effectiveness,<sup>2</sup> however, when exposed to saline solutions, such as cooling liquids, prompt intervention becomes necessary due to significant corrosion issues.<sup>3</sup> Inorganic and organic substances have been explored as potential inhibitors for protecting metals and alloys. Organic

molecules often contain functional groups like -C=N-, -C=O-, C=S, *etc.*, which form covalent bonds involving elements like nitrogen, sulfur, and/or oxygen.<sup>4</sup> Molecules with such characteristics exhibit good inhibitive qualities as they adhere well to steel surfaces, blocking active sites and reducing corrosion rates.<sup>5</sup> The ability of sulfur (S) and nitrogen (N) atoms to form densely confined stable complexes within the coordination range of metal particles has been reported, making them intriguing components for corrosion studies.<sup>6</sup> Transition metal complexes have found extensive applications in various fields, including electrocatalysis,<sup>7</sup> sensing materials,<sup>8</sup> biological probes,<sup>9</sup> and catalysts.<sup>10</sup> Studies on metal complexes containing heterocyclic ligands<sup>11,12</sup> and Schiff bases<sup>13,14</sup> have demonstrated their inhibitory efficacy against corrosion in acidic environments. Mahdavian *et al.*<sup>15</sup> also reported the effectiveness of diverse transition-metal complexes of acetylacetonate in protecting against corrosion. Furthermore, these researchers examined the impact of ligand size on mild steel's resistance to corrosion in zinc complexes.<sup>16</sup>

Hydrazone compounds containing the azomethine group '-CH=N-', have gained significant interest in both combinatorial and medicinal chemistry.<sup>17,18</sup> Their ability to coordinate with

<sup>a</sup>Chemistry Department, Faculty of Science, Mansoura University, Mansoura 35111, Egypt

<sup>b</sup>Department of Chemistry, Faculty of Science, Tanta University, Tanta 31527, Egypt

<sup>c</sup>Department of Chemistry, College of Science and Humanities in Al-Kharj, Prince Sattam Bin Abdulaziz University, Al-Kharj 11942, Saudi Arabia. E-mail: k.shalabi@psau.edu.sa

<sup>d</sup>Delta University for Science and Technology, Gamasa, Mansoura, 11152, Egypt. E-mail: dr.ymostafa8@gmail.com; Yasser\_mostafa@deltauniv.edu.eg

† Electronic supplementary information (ESI) available. See DOI: <https://doi.org/10.1039/d4ra00404c>


ions, adaptability to assume diverse configurations, and consequent applicability in spectrophotometric measurement of transition metals highlight their importance. These compounds can coordinate with metals in either a neutral or anionic state.<sup>19</sup> The presence of multiple donor positions, for example –NNO, in their chemical structure enhances their resistance and limits corrosion damage, making their coordination complexes uniquely designed.<sup>20</sup> Notably, hydrazones have been widely explored as corrosion inhibitors, as evidenced by the popularity of their use in the literature.<sup>21–23</sup> Given this, we decided to investigate the potential of a derivative of hydrazone as a potent inhibitor of steel disintegration in corrosive, acidic environments.<sup>24</sup> While measuring inhibition effectiveness traditionally relies on experimental techniques such as chemical and electrochemical methods,<sup>25</sup> relying solely on these techniques can make it challenging to precisely understand the processes occurring between the metal surface and the investigated compound.<sup>26</sup>

In this investigation, we aimed to assess the effectiveness of a hydrazone derivative and its zinc complex as efficient inhibitors for corrosion on the surface of X70 steel in 3.5% NaCl solutions. The evaluation was carried out with electrochemical techniques, specifically potentiodynamic polarization (PP) and electrochemical impedance spectroscopy (EIS). Additionally, the establishment of a protecting film adsorbed on the steel surface was established by X-ray photoelectron spectroscopy (XPS). To increase more perceptions into the adsorption performance and inhibition mechanisms of the H<sub>2</sub>TTAH and Zn-H<sub>2</sub>TTAH molecules on Fe (1 1 0), we employed Monte Carlo (MC) simulations and density functional theory (DFT) calculations. The goal was to compare the empirical results obtained from experimental techniques with computational findings. Remarkably, a high degree of agreement was observed between the two approaches. The combination of experimental and computational approaches allowed for a comprehensive consideration of the adsorption behavior and mechanisms of inhibition of the hydrazone derivative and its zinc complex on the Fe (1 1 0) surface. This holistic approach enhances our knowledge of the corrosion inhibition progression and affords appreciated perceptions for the design of effective corrosion inhibitors.

## 2. Materials and methods

### 2.1. Composition of material models

In this paper, we utilized a model of API 5L X70 carbon steel, which has the following basic composition in weight percent (wt%): C 0.026, Mn 1.51, Si 0.10, S 0.02, N 0.27, Ni 0.16, Al 0.35, Cr 0.27, Cu 0.28, Nb 0.93, Ti 0.11, and the remaining Fe.

To investigate the corrosion behavior of the carbon steel, we conducted electrochemical methods on a carbon steel disc. The disc was mounted in a Teflon tube, with an exposed area of 1 cm<sup>2</sup>, enabling it to interact with the corrosive medium. For the corrosive solutions, reagent-grade solutions were prepared and diluted to obtain 3.5% NaCl solutions.

By subjecting the carbon steel sample to electrochemical methods in these corrosive solutions, we aimed to analyze and evaluate its corrosion resistance and behavior.

### 2.2. Inhibitors

**2.2.1. Materials and instrumentation.** The chemical compounds and reagents used in the study were of Fluka or Sigma-Aldrich quality, indicating their high purity. The percentages of carbon (C), hydrogen (H), and nitrogen (N) in the compounds were measured utilizing a PerkinElmer 2400 series II analyzer. The metal and chloride contents were assessed using well-established techniques.

Infrared (IR) spectra of the samples were obtained using KBr discs in the range of 4000–400 cm<sup>−1</sup>. A Mattson 5000 FTIR spectrophotometer was employed for this purpose. Electronic spectra were measured using a Unicam UV-Vis spectrophotometer UV2.

The magnetic susceptibility of the samples at 298 K was evaluated using a Sherwood scientific magnetic susceptibility balance.

Nuclear magnetic resonance (NMR) spectra were recorded using CDCl<sub>3</sub> or DMSO-d<sub>6</sub> as the internal reference and solvent, respectively. A Varian V NMR 400 spectrometer performing at 400 MHz for <sup>1</sup>H and 101 MHz for <sup>13</sup>C nuclei was used for NMR analysis.

Electrospray ionization (ESI) mass spectra were obtained using an Orbitrap mass spectrometer manufactured by Thermo Scientific (Rockford, IL, USA).

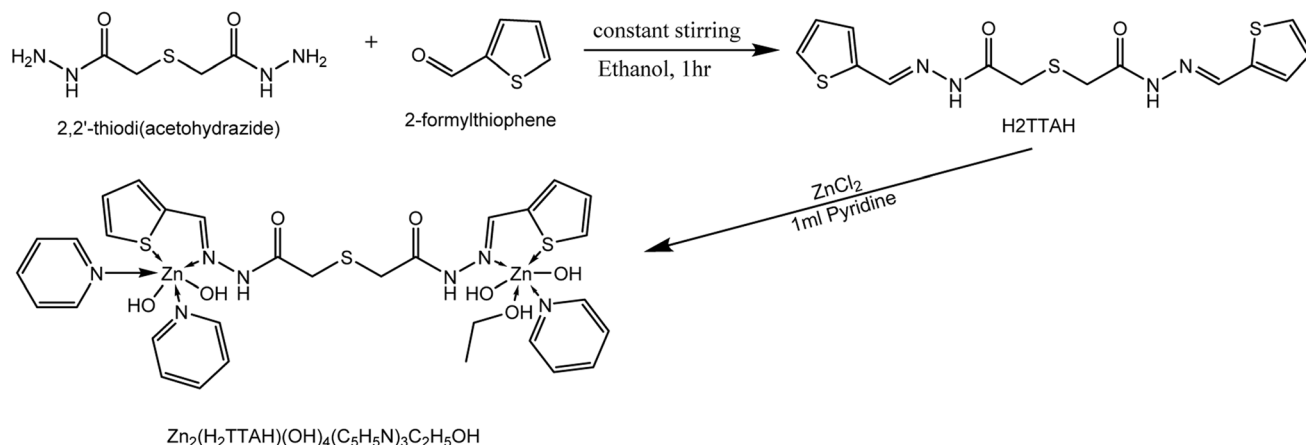
Thermogravimetric analysis (TGA) and differential thermal analysis (DTA) measurements were achieved using a DTG-50 Shimadzu thermogravimetric analyzer. The measurements were carried out in a nitrogen atmosphere with a flow rate of 15 ml min<sup>−1</sup>, and the temperature was amplified at a rate of 10 °C min<sup>−1</sup>.

Electron spin resonance (ESR) spectra were recorded employing a powder ESR spectrometer operating at X-band (9.78 GHz) with a modulation frequency of 100 kHz. The measurements were conducted in a 2 mm quartz capillary at ambient temperature using a Bruker EMX spectrometer.

**2.2.2. Synthesis of H<sub>2</sub>TTAH.** As stated in ref. 27, 2,2'-thiodi(acetohydrazide) (TAH) was created. With steady stirring for an hour (Scheme 1), 50 ml of an ethanolic solution of 2-formylthiophene (2.226 g, 2.54 ml, 0.025 mol) was mixed with 20 ml of aqueous 2,2'-thiodi(acetohydrazide) solution (1.78 g, 0.01 mol). The subsequent white precipitate was sifted out, washed with cold ethanol and water, allowed to air dry, and then was recrystallized from ethanol. TLC was used to determine the hydrazone's (H<sub>2</sub>TTAH) purity, m. p: 210 °C; yield (3.05 g, 88%); IR (KBr)  $\nu$ /cm<sup>−1</sup>: 3358(m,  $\nu$ (OH)), 3226, 3215(m,  $\nu$ (NH)), 1668(s,  $\nu$ (C=O)), 1597 (s,  $\nu$ (C=C)ph), 1563(s,  $\nu$ (C=N)<sub>azo</sub>), 1641 (s,  $\nu$ (C=N\*)<sub>azo</sub>), 1230(s,  $\nu$ (C-O)), 1316 (s,  $\delta$ (OH)), 1132 (s,  $\nu$ (N-N)), 854, 772, 686(s,  $\nu$ (C-S)<sub>thiophen</sub>), 706(s,  $\nu$ (C-S-C)); <sup>1</sup>H NMR (400 MHz, dmsO)  $\delta$ : 11.53 (d,  $J$  = 11.3 Hz, 1H), 11.49 (d,  $J$  = 16.1 Hz, 1H), 8.39 (d,  $J$  = 5.5 Hz, 1H), 8.17 (d,  $J$  = 12.6 Hz, 1H), 7.44–7.39 (m, 4H), 7.13–7.09 (m, 6H), 3.74(dd,  $J$  = 14.4, 1.5 Hz, 2H), 3.37–3.34 ppm (m, 2H); <sup>13</sup>C NMR (101 MHz, dmsO)  $\delta$  170.28, 165.05, 142.05, 138.91, 131.02, 130.32, 130.22, 128.95, 128.91, 128.87, 127.83, 39.93, 33.82, 32.38, 32.04, MS (ESI)  $m/z$  = 366.31 (M<sup>+</sup> + H).

**2.2.3. Synthesis of Zn-H<sub>2</sub>TTAH.** With continual stirring, steaming ethanol suspension of the appropriate ligand (20 ml)



Scheme 1 Synthesis scheme of H<sub>2</sub>ATTH and its Zn-H<sub>2</sub>ATTH.Table 1 Structures, molecular weights and molecular formulas of the synthesized H<sub>2</sub>TTAH and Zn-H<sub>2</sub>TTAH complex

Inhibitor	Chemical structure	Name, molecular weight, chemical formula
H <sub>2</sub> TTAH		2,2'-Thiobis(N'-((E)-thiophen-2-ylmethylene)acetohydrazide) Molecular weight: 366.47 Chemical formula: C <sub>14</sub> H <sub>14</sub> N <sub>4</sub> O <sub>2</sub> S <sub>3</sub>
Zn-H <sub>2</sub> TTAH [Zn <sub>2</sub> (H <sub>2</sub> TTAH)(OH) <sub>4</sub> ·(C <sub>5</sub> H <sub>5</sub> N) <sub>3</sub> C <sub>2</sub> H <sub>5</sub> OH]		Tetrahydroethanoltripyridine(2,2'-thiobis-(N'-((E)-thiophen-2-ylmethylene)acetohydrazide))dizinc(II) Molecular weight: 848.461 Chemical formula: Zn <sub>2</sub> C <sub>31</sub> H <sub>39</sub> N <sub>7</sub> O <sub>7</sub> S <sub>3</sub>

was varied with a hot ethanolic solution of the suitable ZnCl<sub>2</sub> (0.001 mol). The reaction mix received a 1 ml addition of pyridine. Anhydrous CaCl<sub>2</sub> was included in the reaction mixture, which was then vacuum dried for 2 h at 100 °C while being constantly stirred until a precipitate instantly formed (Scheme 1). Table 1 contains the structures, molecular formulae, and molecular weights of the synthesized H<sub>2</sub>TTAH and Zn-H<sub>2</sub>TTAH (Scheme 1).

### 2.3. Electrochemical measurements

The electrochemical workstation CS350's potentiostat/Galvanostat with three electrodes was employed. The API 5L X70 class was used to construct the carbon steel working electrode, which had a 1 cm<sup>2</sup> surface area and was situated extremely near to the reference electrode to reduce the IR drop. The electrode was abraded using emery sheets formerly each trial. Thereafter, the electrode was successively cleansed with ethanol through ultrasonic bath, followed by a rinsing with distilled water. An Ag/AgCl reference electrode was taken into consideration while limiting the potential of the working electrode. A 1 cm<sup>2</sup> platinum sheet was used as the counter electrode. Following thirty minutes of the working electrode

being submerged in the test solution, open circuit potential (OCP) that is steady being attained. The Tafel polarization diagrams were acquired by combining several electrodes under potentiodynamic circumstances comparable to 1 mV s<sup>-1</sup> (sweep rate) in an environment of air. All measurements were made at 25 ± 1 °C using a carbon steel electrode in solutions including 3.5% NaCl, with and without various dosages of the investigated substances. From eqn (1), the inhibitory effectiveness (%η) and surface exposure (θ) were intended:

$$\% \eta = \theta \times 100 = \left[ 1 - \left( \frac{i_{\text{corr(inh)}}}{i_{\text{corr(free)}}} \right) \right] \times 100 \quad (1)$$

The terms "*i*<sub>corr(free)</sub>" and "*i*<sub>corr(inh)</sub>" refer to the corrosion current densities with and without different dosages of investigated compounds, respectively.

The cell used for the polarization experiments was also utilized for the electrochemical impedance spectroscopy (EIS) results. The EIS calculations were accomplished with a perturbed signal amplitude of 10 mV over a frequency variety of 0.01 Hz to 100 kHz. Eqn (2) was applied to assess the inhibitory



competence ( $\% \eta$ ) and surface coverage ( $\theta$ ) of the molecules under investigation.

$$\% \eta = \theta \times 100 = \left[ \left( \frac{R_{ct} - R_{ct}^0}{R_{ct}} \right) \right] \times 100 \quad (2)$$

The charge transfer resistance values, denoted as  $R_{ct}^0$  and  $R_{ct}$ , characterize the resistance in presence and without the inhibitor doses, correspondingly.

#### 2.4. Surface investigations (X-ray photoelectron spectroscopy (XPS))

The high-resolution X-ray photoelectron spectroscopy (XPS) analyses of inhibited API 5L X70 C-steel samples in 3.5% NaCl solution with  $1 \times 10^{-4}$  M of **H<sub>2</sub>TTAH** and **Zn-H<sub>2</sub>TTAH** at  $25 \pm 1^\circ$  C were shown using Thermo Fisher Scientific's K-ALPHA (Thermo Fisher Scientific, USA).

#### 2.5. Theoretical computations

Density Functional Theory (DFT) computations were achieved by applying the Dmol<sup>3</sup> module within the BIOVIA Materials Studio software, version 2017. The methodological approach incorporated B<sub>3</sub>LYP functional coupled with DNP 4.4 basis set. These analytical procedures centered on the optimization of the total energy of both **H<sub>2</sub>TTAH** and **Zn-H<sub>2</sub>TTAH** molecules under aqueous conditions.<sup>28</sup> The results of DFT calculations were considered and determined as follows in the next calculations,<sup>29</sup> taking into account the dipole moment ( $\mu$ ), the energy gap ( $\Delta E$ ), electronegativity ( $\chi$ ), chemical hardness ( $\eta$ ), global softness ( $\sigma$ ), electrophilicity index ( $\omega$ ), the number of electrons transported ( $\Delta N$ ) and back-donation energy ( $E_{\text{back-donation}}$ )

$$\chi = \frac{-E_{\text{HOMO}} - E_{\text{LUMO}}}{2} \quad (3)$$

$$\eta = \frac{1}{\sigma} = \frac{E_{\text{LUMO}} - E_{\text{HOMO}}}{2} \quad (4)$$

$$\omega = \frac{\chi^2}{2\eta} \quad (5)$$

$$\Delta N = \frac{\phi - \chi_{\text{inh}}}{2(\eta_{\text{Fe}} - \eta_{\text{inh}})} \quad (6)$$

$$\Delta E_{\text{back-donation}} = \frac{-\eta}{4} \quad (7)$$

The function work of Fe (1 1 0) is represented by  $\phi$ , while the inhibitor electronegativity is denoted by  $\chi_{\text{inh}}$ .  $\eta_{\text{Fe}}$  and  $\eta_{\text{inh}}$  represent the chemical hardness of Fe (0 eV) and the investigated compounds, respectively. To ascertain the most optimal configurations for adsorption of **H<sub>2</sub>TTAH** and **Zn-H<sub>2</sub>TTAH** molecules on the Fe (1 1 0) surface, the adsorption locator module within Materials Studio version 2017 was employed. This assessment utilized the COMPASS force field to refine the molecular structure of the adsorbates.<sup>30</sup> Subsequently, a computational representation involving the interaction of **H<sub>2</sub>TTAH** and the **Zn-H<sub>2</sub>TTAH** molecules as well as Cl<sup>−</sup> ions, H<sub>3</sub>O<sup>+</sup> ions, and H<sub>2</sub>O particles with the Fe (1 1 0) surface was executed within a dimension of a simulation box of 37.24 Å × 37.24 Å × 59.81 Å.

### 3. Results and discussion

#### 3.1. Investigated inhibitors characterization

The proposed structural formulae were decided on the basis of the collected elemental and spectral measurements (Table 2). The molar conductivity of the Zn(II) chelates ( $\Lambda_m = 5.09 \text{ ohm}^{-1} \text{ cm}^2 \text{ mol}^{-1}$ ) signifying non-electrolytic feature.

**3.1.1. IR, <sup>1</sup>HNMR and <sup>13</sup>CNMR spectral characterization.** IR peaks of the bishydrazone, **H<sub>2</sub>TTAH**, (structure 1) and its **Zn-H<sub>2</sub>TTAH** (structure 2) complex are presented (S.1a-b & Table 3). An insight to the infrared spectrum of **H<sub>2</sub>TTAH** gives an indication that there are two tautomeric forms (keto-enol)

Table 2 Elemental examination and physical information of **H<sub>2</sub>TTAH** and **Zn-H<sub>2</sub>TTAH** complex

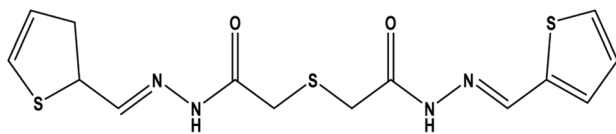
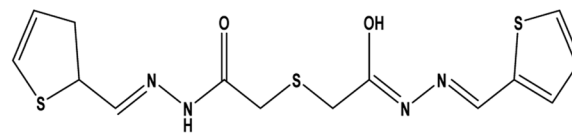
Compound	M.wt	Color	M.p	Found (calc.) %					Yield %
				C%	H%	N%	M%	Cl%	
<b>H<sub>2</sub>TTAH</b> C <sub>14</sub> H <sub>14</sub> N <sub>4</sub> O <sub>2</sub> S <sub>3</sub>	366.31 (366.47)	Yellowish white	210	45.82 (45.88)	3.82 (3.85)	15.26 (15.28)	—	—	80
[Zn <sub>2</sub> (H <sub>2</sub> TTAH)(OH) <sub>4</sub> (C <sub>5</sub> H <sub>5</sub> N) <sub>3</sub> C <sub>2</sub> H <sub>5</sub> OH]	848.461	Yellowish white	180	43.87 (44.04)	4.04 (4.24)	11.55 (11.17)	—	15.40 (15.00)	68
Zn <sub>2</sub> C <sub>31</sub> H <sub>39</sub> N <sub>7</sub> O <sub>7</sub> S <sub>3</sub>									

Table 3 Assignments of the representative infrared spectral peaks of **H<sub>2</sub>TTAH** and **Zn-H<sub>2</sub>TTAH** complex

Compound	$\nu$ (OH)	$\nu$ (NH)	$\nu$ (C=O)	$\nu$ (C=N)*	$\nu$ (C=N) <sub>azo</sub>	$\nu$ (C-O)	$\nu$ (N-N)	$\nu$ (C-S) <sub>thio</sub>	$\nu$ (M-O)	$\nu$ (M-S)	$\nu$ (M-N)
<b>H<sub>2</sub>TTAH</b>	—	3226	1686	1641	1563	1230	1080	854 772 686	—	—	—
<b>Zn-H<sub>2</sub>TTAH</b>	3437	3228	1686	1599	1522	1217	1135	503	430		436





**H<sub>2</sub>TTAH (a) (29%)****H<sub>2</sub>TTAH (b) (71%)**Scheme 2 The two tautomeric forms (keto–enol) of H<sub>2</sub>ATTH.

(Scheme 2) comprise a  $\sim 1 : 2$  molar ratio, revealed by a doublet band observed at 1686 and 1641  $\text{cm}^{-1}$  due to the stretching vibration mode of the (C=O) group<sup>31</sup> which is supported by two signals in the  $^1\text{H}$  NMR (in DMSO- $d_6$ ) spectrum (**S.2a**) of the ligand assignable to the keto form (**1a**) at 11.45 ppm (NH), 8.14 ppm (azomethine protons), and 3.74 ppm (–COCH<sub>2</sub>–S– protons) and at 11.52 ppm (C(OH)=N proton), a more deshielded azomethine proton at 8.17, and a more shielded S–CH<sub>2</sub> group at 3.75 ppm arising due to those characteristic for enol form (**1b**). In addition to the duplication of signals of all hydrogen as those due to the aromatic protons appeared as two multiplets at 7.39 and 7.65 ppm. In addition, the two signals observed at 170.28 (C(OH)=N carbon) and 170.12 (C=O, carbon) ppm, with the duplication of the other signals in the  $^{13}\text{C}$  spectra of the ligand H<sub>2</sub>TTAH (**S.2b**) are further evidence for the suggestion of such tautomerization of H<sub>2</sub>TTAH in solutions. This remains more established by the DFT molecular model of the ligand as the two suggested isomers revealing a significant variation in the total energy between keto (3997.53  $\text{kcal mol}^{-1}$ ) and enol (4007.38  $\text{kcal mol}^{-1}$ ) forms, respectively. The band at 1532  $\text{cm}^{-1}$  is characteristic for  $\nu(\text{C}=\text{N})_{\text{azomethine}}$  vibration undergoes a blue shift upon complex formation. The two bands at 1597 and 1132  $\text{cm}^{-1}$  are due to  $\nu(\text{C}=\text{C})_{\text{ph}}$  and  $\nu(\text{N}=\text{N})$  modes of vibration. The broad band detected at 3226 and a shoulder joint at 3215  $\text{cm}^{-1}$  of the two isomers are ascribed to  $\nu(\text{NH})$  vibration of the two systems in the solid-state.<sup>31</sup> The band at 686  $\text{cm}^{-1}$  is attributed to  $\nu(\text{C}=\text{S})_{\text{thiophene}}$  whereas that at 706  $\text{cm}^{-1}$  is attributed to  $\nu(\text{C}=\text{S}=\text{C})$  vibrational mode. These bands undergo shift and a new peak corresponding to  $\nu(\text{M}=\text{S})$  appeared as the combination of S-thiophene moiety in coordination occurred.<sup>31</sup> H<sub>2</sub>TTAH acted as a NNSS-neutral tetradentate in  $[\text{Zn}_2(\text{TTAH})(\text{OH})_2(\text{C}_5\text{H}_5\text{N})_2(\text{C}_2\text{H}_5\text{OH})_2]$  complex (structure 2) where it bounded to two Zn(II) ions *via* the two azomethine-N and the two thiophene-S atoms.

The suggested approach of chelation is established on comparing the IR spectrum of the hydrazone with that of the Zn(II) complex (**S.1b**) as follows:

(i) There is no notified variation in the position and/or energy of the absorption bands ascribed to  $\nu(\text{NH})$  and  $\nu(\text{C}=\text{O})$  proving nonsharing in coordination.

(ii) The clear blue shift in the bands owing to azomethine  $\nu(\text{C}=\text{N})_{\text{azo}}$  and  $\nu(\text{N}=\text{N})$  modes.<sup>32</sup>

(iii) The coordination through thiophene-S is revealed by the alteration in both the intensity and the position of the characteristic peaks of thiophene ring from (854, 772 and 686)  $\text{cm}^{-1}$  to (854, 759, 637)  $\text{cm}^{-1}$ .<sup>33</sup>

(iv) The complex spectra of  $\nu(\text{Zn}=\text{O})$  and  $\nu(\text{Zn}=\text{N})$  showed the emergence of new bands at (503–568)  $\text{cm}^{-1}$  and (430–453)  $\text{cm}^{-1}$ .<sup>34</sup>

(v) The coordination of pyridine nitrogen is confirmed by the newly identified bands at (1600–1615), (986–1009) and (758)  $\text{cm}^{-1}$ , which are attributed to  $\nu(\text{C}=\text{N})$  stretching, pyridine ring breathing, in-plane-bending, and out-of-plane ring vibration modes, respectively.

(vi) The ethanol molecule's  $\delta(\text{OH})$  and  $\nu(\text{OH})$  are responsible for the bands in the IR-spectrum of the Zn(II) complex that are centered at 3393  $\text{cm}^{-1}$  and (1322–1382)  $\text{cm}^{-1}$ . The ethanol coordination is further reinforced by the identification of bands corresponding to  $\nu(\text{M}=\text{O})$  at 476–459  $\text{cm}^{-1}$ .

**3.1.2. Mass spectral data.** Electrospray ionization (ESI) mass spectrometry (**S.3**) has verified the H<sub>2</sub>TTAH hydrazone under investigation's formula weight. All ligands' parent peak  $m/z$  has been identified as ( $\text{M}^+ + \text{H}$ ). This information agrees with the known chemical formula and the findings of the partial elemental investigation shown in Table 2. Additionally, the purity of the produced compound is shown by the sharp melting point.

**3.1.3. Electronic spectral characterization.** The electronic spectrum of H<sub>2</sub>TTAH was seen in Nujol mull (**S.4**) or dimethylformamide (DMF) solution. Two strong bands in the ligand spectra, at 308 and 344 nm, were ascribed to  $\pi \rightarrow \pi^*$  of azomethine and carbonyl groups, respectively. The coordination of the azomethine nitrogen and carbonyl oxygen atoms with the essential metal ion is supported by a significant shift in these bands' Zn(II) complex towards higher frequencies. The two ( $n \rightarrow \pi^*$ ) of the carbonyl group's additional bands are attributed to it at 349 nm.<sup>33</sup> Also, the absorption band at 358 nm may be attributed to LMCT.

### 3.2. Potentiodynamic polarization method (PP)

Fig. 1 and 2 describes the Tafel diagrams for X70 carbon steel in 3.5% NaCl medium and using various dosages of investigated compounds from  $1 \times 10^{-6}$  M to  $1 \times 10^{-4}$  M. Table 4 involves the equivalent electrochemical variables consequent from the PP plots. The values that are typically measured and used to assess corrosion are the corrosion potential ( $E_{\text{corr}}$ ), corrosion current density ( $i_{\text{corr}}$ ), cathodic Tafel slope ( $\beta_c$ ), and anodic Tafel slope ( $\beta_a$ ). Additionally, the inhibition proficiency ( $\eta$  %) can be calculated using eqn (1).<sup>34</sup>

The Tafel plots show that as the concentration of H<sub>2</sub>TTAH augmented, the corrosion current densities,  $i_{\text{corr}}$ , diminished for anodic and cathodic branches. These results confirm that the H<sub>2</sub>TTAH and Zn-H<sub>2</sub>TTAH inhibitors have inhibitory properties on the anodic and cathodic directions. The statistics presented in Table 4 showed a slight increase in the corrosion



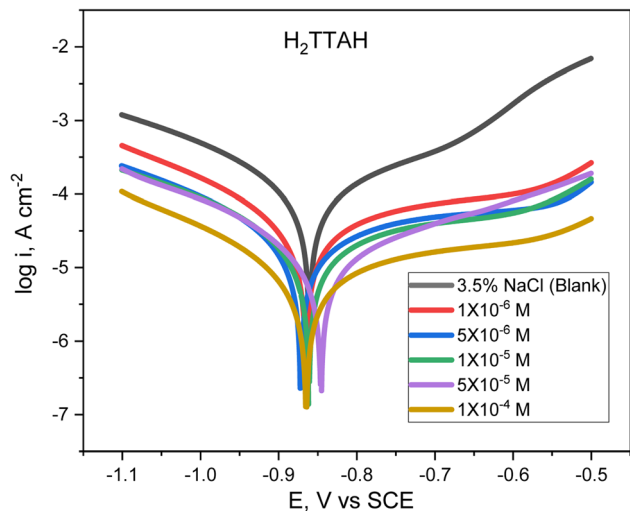


Fig. 1 Cathodic and anodic Tafel plots for API 5L X70 C-steel samples in 3.5% NaCl solution treated with altered dosages of  $\text{H}_2\text{TTAH}$ , at  $25 \pm 1^\circ\text{C}$ .

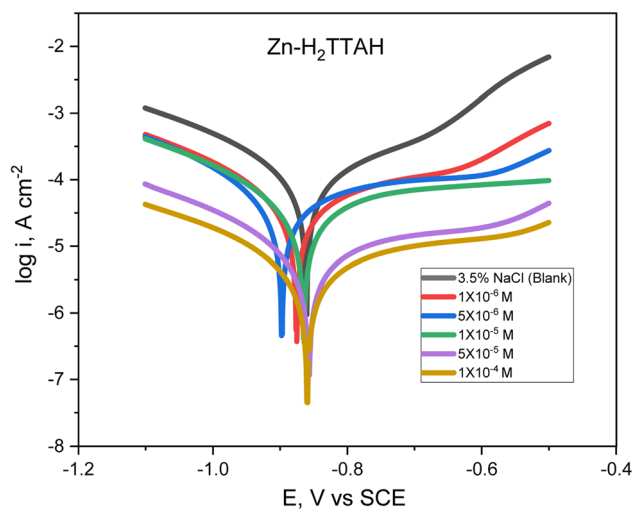


Fig. 2 Tafel plots for API 5L X70 C-steel in 3.5% NaCl solution treated with several dosages of  $\text{Zn-H}_2\text{TTAH}$ , at  $25 \pm 1^\circ\text{C}$ .

potentials ( $E_{\text{corr}}$ ) related to the 3.5% NaCl solution by  $<-85$  mV. Consequently, this observation can be attributed to the mixed type properties of  $\text{H}_2\text{TTAH}$  and  $\text{Zn-H}_2\text{TTAH}$  inhibitors.<sup>35</sup>

Furthermore, the rise in the inhibitors concentrations resulted in insignificant alterations in the anodic and cathodic Tafel slopes ( $\beta_a$  and  $\beta_c$ ), which suggests that the corrosion mechanism during the dissolution and oxygen reduction processes remained unaltered by the inhibitors under investigation.<sup>36</sup> This discovery validates the inhibitors' mixed-type characteristics.

The polarization findings designate that  $\text{H}_2\text{TTAH}$  and  $\text{Zn-H}_2\text{TTAH}$  inhibitors have superior inhibition performance (*i.e.*, smallest  $i_{\text{corr}}$  value) at a concentration of  $1 \times 10^{-4}$  M compared to other test solutions. According to  $i_{\text{corr}}$  values (Table 4), we can conclude that  $\text{Zn-H}_2\text{TTAH}$  exhibits greater potential for inhibiting corrosion compared to  $\text{H}_2\text{TTAH}$  (*i.e.*, smaller  $i_{\text{corr}}$ ) because the  $\text{Zn-H}_2\text{TTAH}$  complex has larger size and molecular planarity, as well as the existence of three extra pyridine rings in the  $\text{Zn-H}_2\text{TTAH}$  complex in comparison with  $\text{H}_2\text{TTAH}$  structure, which indicates a greater inclination to donate electrons, which accounts for its superior inhibitory effectiveness. Two inhibitors have the capability to retard the corrosion process of steel by adhering to active positions and constructing a protecting layer.

### 3.3. Electrochemical impedance spectroscopy (EIS)

The Nyquist diagrams in Fig. 3(A) and (B) display the Nyquist designs for X70 steel corrosion in 3.5% NaCl solutions at  $25 \pm 1^\circ\text{C}$ , using various dosages of evaluated inhibitors.

The corrosion inhibition mechanism of  $\text{H}_2\text{TTAH}$  or  $\text{Zn-H}_2\text{TTAH}$  is explored. The Bode plots shown in Fig. 4(A) and (B) confirm a consistent rise in phase angle shift as the concentrations of examined inhibitors increase. These inhibitors adsorbed on the steel examined metal, resulting in its creation of a high-frequency capacitive loop. Plots display a semicircle pattern that grows larger as concentrations rise.<sup>37</sup> It is evident that the corrosion process exhibited by the inhibited X70 steel in a 3.5% NaCl solution is, to a certain degree, influenced by mass transport phenomena (*i.e.*, diffusion) as evidenced by the presence of Warburg impedance at intermediate and low frequency ranges.

Table 4 The potentiodynamic polarization approach yielded electrochemical variables for the corrosion of X70 steel in 3.5% NaCl solution, both in the presence and absence of varying dosages of the studied  $\text{H}_2\text{TTAH}$  and  $\text{Zn-H}_2\text{TTAH}$  complex at  $25 \pm 1^\circ\text{C}$

Comp.	Conc., M	$-E_{\text{corr}}$ , mV	$i_{\text{corr}}$ , $\mu\text{A cm}^{-2}$	$\beta_a$ , mV dec $^{-1}$	$\beta_c$ , mV dec $^{-1}$	C.R. mm per year	$\theta$	$\eta$ , %
3.5% NaCl (0.6 M)		861.4	70.86	212.82	154.94	1.1425	—	—
I; $\text{H}_2\text{TTAH}$	$1 \times 10^{-6}$	869.5	35.02	275.61	134.39	0.405	0.506	50.6
	$5 \times 10^{-6}$	878.9	15.39	290.83	147.75	1.783	0.783	78.3
	$1 \times 10^{-5}$	866.2	11.61	271.92	136.99	1.345	0.836	83.6
	$5 \times 10^{-5}$	843.7	10.22	246.48	162.80	1.184	0.856	85.6
	$1 \times 10^{-4}$	868.8	4.70	275.55	136.46	0.545	0.934	93.4
II; $\text{Zn-H}_2\text{TTAH}$	$1 \times 10^{-6}$	880.0	27.99	263.35	141.11	3.24	0.605	60.5
	$5 \times 10^{-6}$	890.1	24.70	209.07	139.35	2.86	0.651	65.1
	$1 \times 10^{-5}$	863.1	22.22	263.39	150.81	2.57	0.686	68.6
	$5 \times 10^{-5}$	858.7	4.49	268.70	145.69	0.96	0.937	93.7
	$1 \times 10^{-4}$	852.8	2.73	225.46	166.74	0.57	0.961	96.1

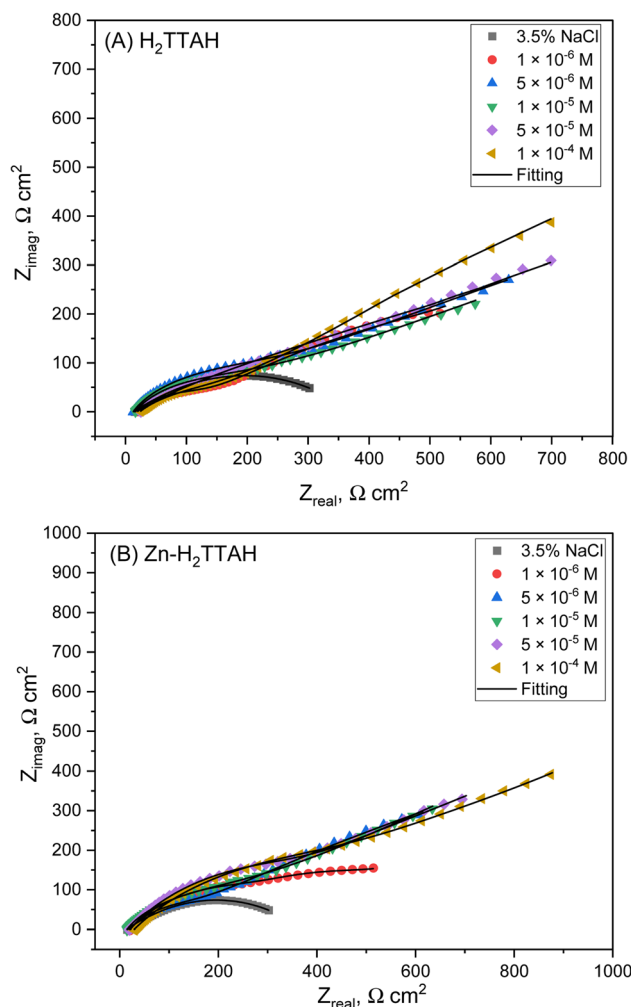


Fig. 3 Nyquist plots for X70 steel corrosion in 3.5% NaCl solution, (A) consuming  $H_2TTAH$ , (B) consuming  $Zn-H_2TTAH$  at  $25 \pm 1^\circ C$ .

In order to fully comprehend the EIS results obtained for X70 steel with different concentrations of  $H_2TTAH$  or  $Zn-H_2TTAH$ , the equivalent circuit (EC) models employed as illustrated in Fig. 5(A) and (B). The fidelity of the model, assessed through the chi-square ( $\chi^2$ ) goodness of fit, was listed in Table 5 and the fitting results were shown in Fig. 3 and 4. These EC models encompass  $R_s$  (solution resistance),  $R_p$  [polarization resistance;  $R_p = R_f$  (film resistance) +  $R_{ct}$  (charge transfer resistance)],  $CPE_f$  (constant phase element associated with the film),  $CPE_{dl}$  pertaining to electrical double layer and  $W$  (Warburg impedance) particularly in instances involving inhibited samples.

The parameters provided in Table 5 designate that the corrosion behavior of X70 steel in 3.5% NaCl media exhibits semicircle, this may be credited to the irregularity of the steel surface, frequency diffusion, and some mass transfer.<sup>38</sup>

The inhibitory efficiency for the corrosion of X70 steel ( $\% \eta$ ) in a 3.5% NaCl solution can be calculated by the formulae that incorporate the polarization resistance ( $R_p$ ).<sup>39</sup>

$$R_p = R_f + R_{ct} \quad (8)$$

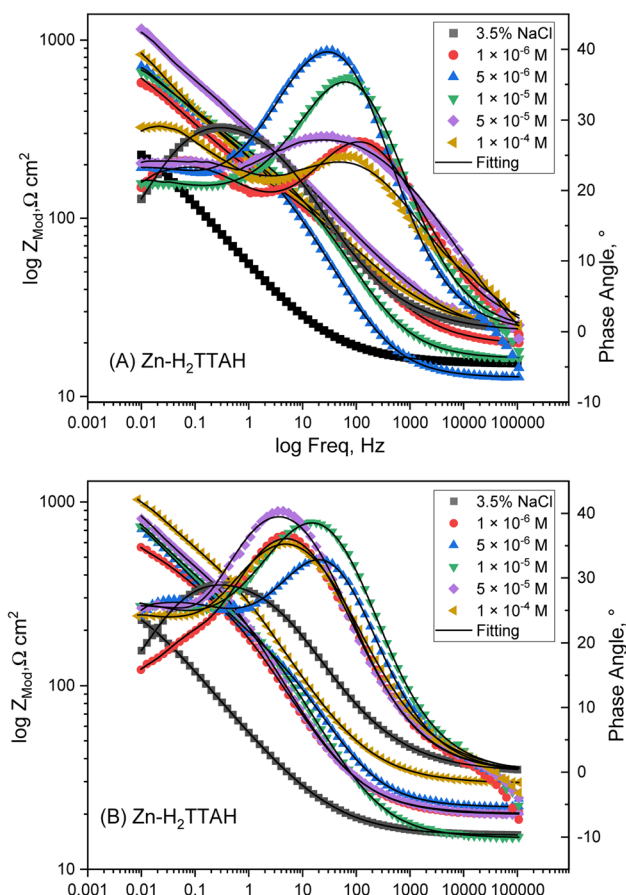


Fig. 4 Bode plots for X70 steel corrosion in 3.5% NaCl solution, (A) consuming  $H_2TTAH$ , (B) consuming  $Zn-H_2TTAH$  at  $25 \pm 1^\circ C$ .

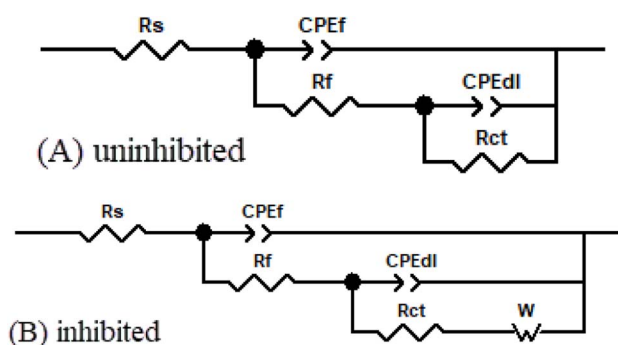


Fig. 5 Electrical corresponding circuit used to fit the X70 steel impedance data in 3.5% NaCl solutions for (A) uninhibited (B) inhibited solutions.

$$\%IE = \theta \times 100 = \left(1 - \left[\frac{R_p^0}{R_p}\right]\right) \quad (9)$$

The polarization resistances of X70 steel in 3.5% NaCl solutions with and in the lack of investigated compounds are  $R_p^0$  and  $R_p$ , correspondingly.



**Table 5** The electrochemical variables of 3.5% NaCl with and without different concentrations of H<sub>2</sub>TTAH and Zn-H<sub>2</sub>TTAH complex at 25 ± 1 °C were obtained from the EIS corresponding circuit suitable for X70 steel

Comp.	Conc., M	CPE <sub>f</sub>			CPE <sub>dl</sub>			R <sub>ct</sub> , Ω cm <sup>2</sup>	R <sub>p</sub> , Ω cm <sup>2</sup>	W, Ω cm <sup>2</sup>	χ <sup>2</sup> × 10 <sup>-3</sup>	θ	%η
		R <sub>s</sub> , Ω cm <sup>2</sup>	Y <sub>0</sub> × 10 <sup>-3</sup> , Ω <sup>-1</sup> s <sup>n</sup> cm <sup>-2</sup>	n	R <sub>f</sub> , Ω cm <sup>2</sup>	Y <sub>0</sub> × 10 <sup>-3</sup> , Ω <sup>-1</sup> s <sup>n</sup> cm <sup>-2</sup>	n						
3.5% NaCl (0.6 M)		15.3	7.423	0.508	50.8	7.215	0.509	200.2	251.0	—	2.96	—	—
<b>I; H<sub>2</sub>TTAH</b>	1 × 10 <sup>-6</sup>	19.5	0.512	0.497	67.4	4.223	0.503	456.4	523.8	1.85	1.82	0.521	52.1
	5 × 10 <sup>-6</sup>	12.8	0.435	0.629	72.4	1.717	0.494	619.3	691.7	1.92	4.52	0.637	63.7
	1 × 10 <sup>-5</sup>	16.4	0.294	0.610	92.2	0.885	0.485	883.1	975.3	3.34	2.60	0.743	74.3
	5 × 10 <sup>-5</sup>	24.7	0.153	0.502	120.8	0.464	0.424	1332.3	1453.1	3.70	4.69	0.827	82.7
	1 × 10 <sup>-4</sup>	23.5	0.074	0.489	173.0	0.173	0.503	2977.4	3150.4	3.93	4.59	0.920	92.0
<b>II; Zn-H<sub>2</sub>TTAH</b>	1 × 10 <sup>-6</sup>	19.9	0.512	0.553	76.5	1.482	0.437	675.8	752.3	1.02	8.82	0.666	66.6
	5 × 10 <sup>-6</sup>	21.7	0.388	0.519	96.2	4.149	0.429	1140.9	1237.1	1.15	2.9	0.797	79.7
	1 × 10 <sup>-5</sup>	14.9	0.175	0.618	109.1	2.121	0.419	1814.6	1923.7	2.25	4.19	0.870	87.0
	5 × 10 <sup>-5</sup>	20.2	0.044	0.633	162.5	0.430	0.414	3045.9	3208.4	3.36	4.78	0.922	92.2
	1 × 10 <sup>-4</sup>	29.3	0.012	0.532	193.4	0.132	0.405	4752.7	4946.1	8.05	2.29	0.949	94.9

The total impedance  $Z_{CPE}$  can be calculated *via* the next equation:<sup>40</sup>

$$Z_{CPE} = \frac{1}{Y_0(j\omega)^n} \quad (10)$$

The CPE admission, denoted as  $Y_0$ , is determined by several factors. The imaginary number,  $j$ , is involved in the calculation, along with the angular frequency ( $\omega$ ) represented by  $2\pi f$ . Another important factor is the CPE index, denoted as  $n$ , which is calculated based on the phase shift. The value of ' $n$ ' is pivotal in defining the nature of the element depicted by the constant phase element (CPE); wherein  $n$  equating to zero corresponds to a resistor, an  $n$  value between 0 and 1 indicates a non-ideal capacitor, and  $n$  equating to unity denotes an ideal capacitor.<sup>41</sup> The deviation from ideal capacitive character, as revealed by the  $n_{dl}$  values ranging from 0.489 to 0.629, is attributable to a multiplicity of influential factors. These include the surface heterogeneity of X70 steel, the migration of charge carriers at energetic sites, the progressive dissolution of metal, the existence of impurities, and the adsorptive interactions of the inhibitory molecules.

Table 5 delineates the electrochemical parameters ascertained from the EIS studies. Elevated charge transfer resistance ( $R_{ct}$ ) magnitudes associated with **H<sub>2</sub>TTAH** and **Zn-H<sub>2</sub>TTAH** suggest that the mitigation of corrosion in steel samples may be accredited to the adsorptive of these inhibitors, displacing the water particles initially present on the steel surface.<sup>42</sup> A marked decrease in the admittance values ( $Y_0$ )<sub>dl</sub> values corresponds to the adsorptive of **H<sub>2</sub>TTAH** and **Zn-H<sub>2</sub>TTAH** on the X70 steel substrate.<sup>43</sup> This adsorption mechanism contributes to an enhanced thickness of the electrical double layer, culminating in the construction of a protecting inhibitive film atop the steel surface. Notably, the EIS data corroborate a superior corrosion protection efficiency of **Zn-H<sub>2</sub>TTAH** compared to **H<sub>2</sub>TTAH**, a finding that is in concordance with the outcomes derived from PP studies.

### 3.4. Adsorption isotherm and comparison with previous studies

Different kinds of adsorption isotherms were explored to learn more near the relationship amongst the **H<sub>2</sub>TTAH** and **Zn-H<sub>2</sub>TTAH** as corrosion inhibitors and the X70 steel metal surface, adsorption characteristics at 25 ± 1 °C using various kinds to determine the most appropriate mechanism from the appropriate adsorption isotherms.

Utilizing PP data and the following equation, the surface exposure ( $\theta$ ) of separately examined inhibitor at various dosages of concentration in 3.5% NaCl medium has been calculated:

$$\frac{C}{\theta} = \frac{1}{K_{ads}} + C \quad (11)$$

whereas ( $C$ ) are concentrations of the examined derivatives inhibitors and ( $K_{ads}$ ) is the equilibrium constant of adsorption process which is associated with standard-free energy of adsorption ( $\Delta G_{ads}^\circ$ ), and eqn (12) might be used to premedicate the adsorption process.<sup>44</sup>

$$K_{ads} = \frac{1}{55.5} \exp\left(\frac{-\Delta G_{ads}^\circ}{RT}\right) \quad (12)$$

The equation is given as: ( $T$ ) represents the absolute temperature in kelvin, ( $R$ ) signifies the gas constant (8.314 J mol<sup>-1</sup> K<sup>-1</sup>), and (55.5) signifies the apparent molar concentration of H<sub>2</sub>O in solution.

It was confirmed that the tested derivatives' adsorption on steel surface (Fig. 6) follows the Langmuir adsorption isotherm by visually evaluating values of ( $\theta$ ) acquired from the PP approach.<sup>43</sup>

The data presented in Fig. 6 indicates that the ( $C/\theta$ ) design, in relation to ( $C$ ), follows a straight line with a correspondence coefficient ( $R^2$ ) greater than 0.99. This demonstrates that the examined inhibitors being studied can be well adsorbed according to the Langmuir adsorption isotherm. By applying eqn (12), the standard free energy of adsorption ( $\Delta G_{ads}^\circ$ ) is calculated to be -41.93 kJ mol<sup>-1</sup> ( $K_{ads} = 4.03 \times 10^5$  L mol<sup>-1</sup>) for **H<sub>2</sub>TTAH** and -42.96 kJ mol<sup>-1</sup> ( $K_{ads} = 6.10 \times 10^5$  L mol<sup>-1</sup>) for **Zn-H<sub>2</sub>TTAH**.





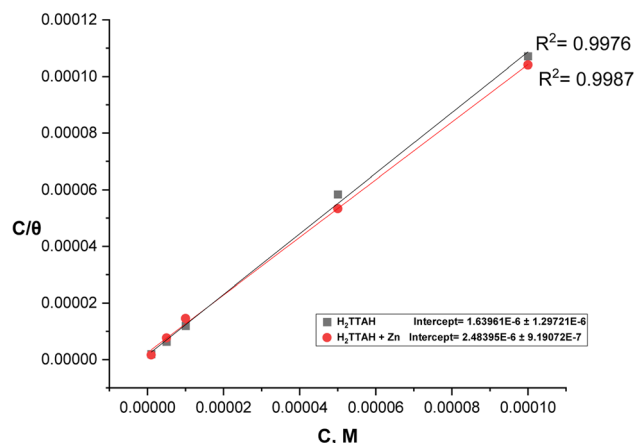


Fig. 6 Langmuir's adsorption diagrams for X70 steel in 3.5% NaCl solutions involving various dosages of investigated inhibitors at  $25 \pm 1^\circ \text{C}$ .

**Zn-H<sub>2</sub>TTAH.** These results suggest that charge transfer arises between the investigated hydrazone compounds and the c-steel surface, resulting in the establishment of a coordinate bond through chemisorption adsorption. The  $\Delta G_{\text{ads}}^\circ$  values show a negative sign, demonstrating that the evaluated compounds are spontaneously adsorbed on the steel surface. Additionally, the high-free energy values, equal to  $-40 \text{ kJ mol}^{-1}$  and higher, further support this observation.<sup>45</sup>

Table 6 demonstrates a comparative study of the inhibition efficiency of the synthesized compounds (**H<sub>2</sub>TTAH** and **Zn-H<sub>2</sub>TTAH**), with various previously reported inhibitors in modifying corrosion of carbon steel within diverse corrosive mediums.<sup>46–55</sup> The results obtained from the PP and EIS studies,

as delineated in Table 6, suggest that **H<sub>2</sub>TTAH** and **Zn-H<sub>2</sub>TTAH**, are efficacious corrosion inhibitors, exhibiting potential for high-performance applications.

### 3.5. XPS studies

The construction and chemical bonds of **H<sub>2</sub>TTAH** and **Zn-H<sub>2</sub>TTAH** on steel surfaces were considered using X-ray photoelectron spectroscopy (XPS). Additionally, the examination aimed to confirm the adsorption of investigated particles on the carbon steel surface. Fig. 7 and 8 present the XPS spectra attained for the X70 carbon steel surface preserved with **H<sub>2</sub>TTAH** and **Zn-H<sub>2</sub>TTAH** inhibitors in a 3.5% NaCl solution at  $25 \pm 1^\circ \text{C}$ . The spectra for the inhibited specimens revealed characteristic peaks for C 1s, Cl 2p, Fe 2p, O 1s, N 1s, and S 2p. Additionally, a peak related to Zn 2p was observed for the specimen treated with the **Zn-H<sub>2</sub>TTAH** complex, providing further evidence of the adsorption of **H<sub>2</sub>TTAH** and **Zn-H<sub>2</sub>TTAH** inhibitors on the surface of API 5L X70 carbon steel. Table 7 presents the binding energies (BE, eV) and conforming assignments for each peak constituent.

The spectrum of C 1s can be separated into two peaks (Fig. 7 and 8) for samples preserved with **H<sub>2</sub>TTAH** and **Zn-H<sub>2</sub>TTAH** inhibitors, the peaks correspond to C–H–, C–C–, and C–Cl bonds at 285.08 and 285.01 eV, and C–N<sup>+</sup> bonds at 288.51 and 288.67 eV.<sup>56,57</sup> The presence of a chlorine peak on API 5L X70 carbon steel specimens treated with **H<sub>2</sub>TTAH** and **Zn-H<sub>2</sub>TTAH** inhibitors in a 3.5% NaCl solution is assigned to the interaction of chloride ions with steel surface which possess positive charge.<sup>58</sup> The Cl 2p spectra of the inhibited specimens showed two peaks at 198.41 and 199.66 eV, for Cl 2p<sub>3/2</sub>, as well as additional peaks at 200.47 and 200.98 eV, for Cl 2p<sub>1/2</sub>, which accredited to Cl–Fe bond in FeCl<sub>3</sub>.<sup>59</sup> The XPS spectra of Fe 2p in

Table 6 Comparison of the as-synthesized bishydrazone's inhibition effectiveness with that of a few other approved inhibitors for the carbon steel electrode under various corrosive conditions

No.	Inhibitor	Corrosive media	Technique	Optimum concentration	$\eta\%$	Ref.
1	Hydrazone compound: HTH	1.0 M HCl	PP	$10^{-3} \text{ M}$	98	46
2	Benzoquinoline derivatives	1.0 M HCl	PP	500 ppm	90.3	47
3	Thiocarbohydrazones based on adamantane and ferrocene	1.0 M HCl	PP	200 ppm	93.6	48
4	Naproxen-based hydrazones	1.0 M HCl	Weight loss EIS	$5 \times 10^{-3} \text{ M}$	90.6 89.2	49
5	Two malonyl dihydrazide derivatives	1.0 M HCl	EIS	$2.0 \times 10^{-5} \text{ M}$	90.7	50
6	Imine compound (PTM) and its cobalt complex (CoPTM)	1.0 M HCl	EIS	2 mM	84.6	51
7	Zn(II) Schiff base complexes	15% HCl	EIS	$0.2 \text{ g L}^{-1}$	87.3	52
8	Hydrazone derivative (HIND)	Concrete pore solutions	Weight loss	0.5 mM	88.4	53
9	Hydrazones derived from thiophene derivatives	0.5 M H <sub>2</sub> SO <sub>4</sub>	Weight loss PP EIS	400 ppm	97.2 94.6 96.3	54
10	N-(5-((4-Chlorophenyl)diazanyl)-2-hydroxybenzylidene)-2-hydroxybenzo hydrazide (CDHBHZ)	1.0 M HCl 0.5 M H <sub>2</sub> SO <sub>4</sub>	Weight loss Weight loss	0.03 M	96.0 89.0	55
13	Bishydrazone ligand and its Zn- complex	3.5% NaCl solution	PP EIS	$1 \times 10^{-4} \text{ M}$	93.4 96.1 93.0 95.6	The present work



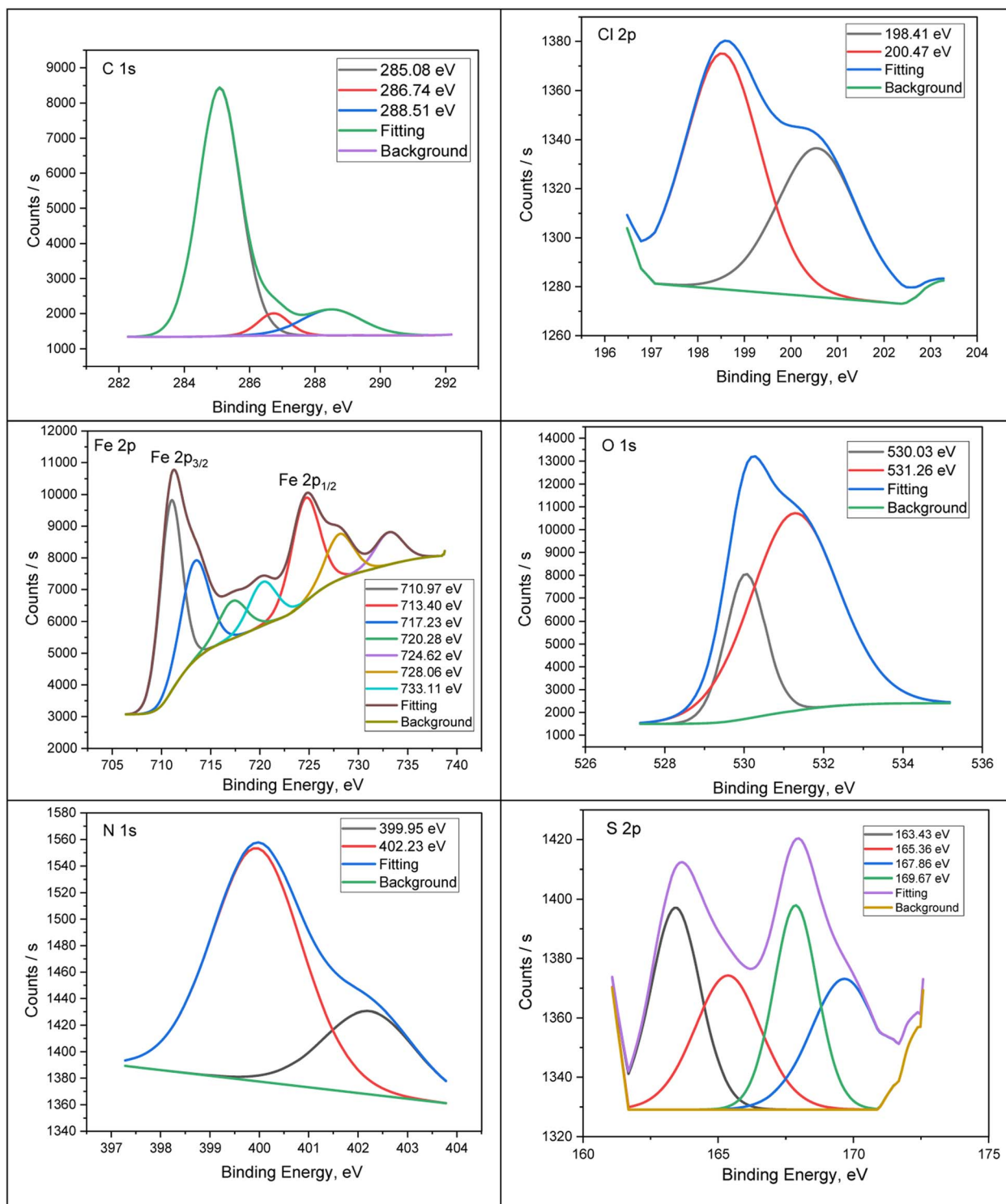
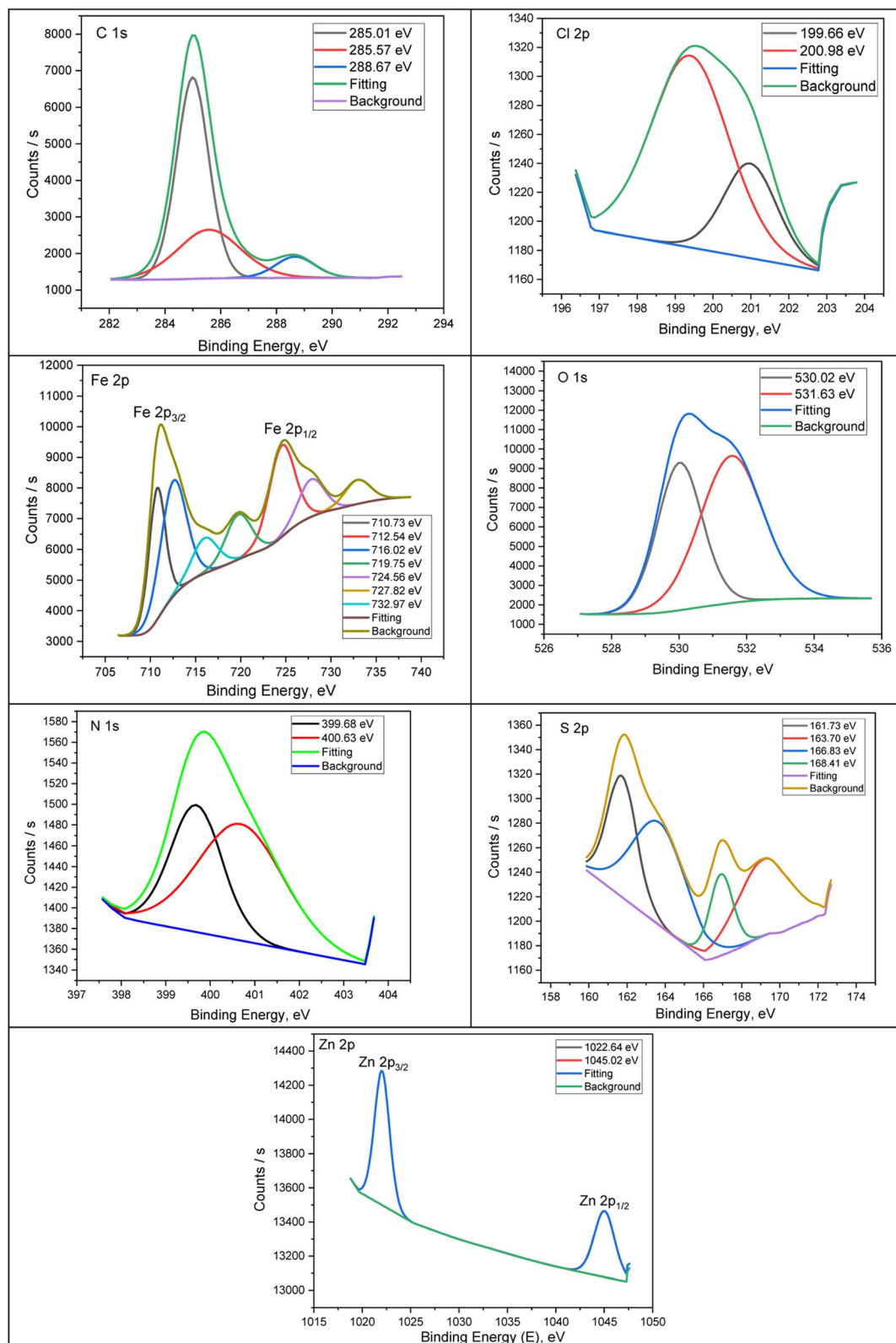


Fig. 7 XPS deconvoluted outlines of C 1s, Cl 2p, Fe 2p, O 1s, N 1s, and S 2p for API 5L X70 C-steel samples in 3.5% NaCl solution treated with  $1.0 \times 10^{-4}$  M of  $\text{H}_2\text{TTAH}$  at  $25 \pm 1^\circ\text{C}$ .

the inhibited specimens exhibited seven peaks. These peaks were assigned to Fe  $2p_{3/2}$  of  $\text{Fe}^{2+}$  at 710.97 and 710.73 eV, Fe  $2p_{3/2}$  of  $\text{Fe}^{3+}$  at 713.40 and 712.54 eV, Fe  $2p_{3/2}$  satellites of  $\text{Fe}^{2+}$  at 720.28 and 719.75 eV, and Fe  $2p_{1/2}$  of  $\text{Fe}^{2+}$  at 724.62 eV.<sup>60,61</sup> Furthermore, in the high-resolution O 1s spectrum, there are two distinct peaks observed (Fig. 7 and 8) for the specimens

treated with  $\text{H}_2\text{TTAH}$  and  $\text{Zn-H}_2\text{TTAH}$  inhibitors. The first peak, at 530.03, 530.02 eV, is recognized to  $\text{O}^{2-}$  and can be associated with oxygen atoms attached to  $\text{Fe}^{2+}$  and  $\text{Fe}^{3+}$  in the FeO and  $\text{Fe}_2\text{O}_3$  oxides.<sup>62</sup> The second peak, at 531.26, 531.63 eV, is accredited to  $\text{OH}^-$  and may be linked to  $\text{Fe}^{3+}$  in  $\text{FeOOH}$ .<sup>63,64</sup>





**Fig. 8** XPS deconvoluted profiles of C 1s, Cl 2p, Fe 2p, O 1s, N 1s, S 2p and Zn 2p for API 5LX70 C-steel samples in 3.5% NaCl solution treated with  $1.0 \times 10^{-4}$  M of Zn-H<sub>2</sub>TTAH  $25 \pm 1$  °C.

Additionally, the N 1s spectrum of the API 5L X70 C-steel in 3.5% NaCl solution containing H<sub>2</sub>TTAH and Zn-H<sub>2</sub>TTAH inhibitors displays two peaks (Fig. 7 and 8). The first peak, at

399.95, 399.68 eV, agrees to  $\text{C}=\text{N}^-$  in inhibitors molecules and formation of N-Fe bond.<sup>65</sup> The second peak 4002.23, 400.63 eV corresponds to protonated nitrogen atoms ( $\text{C}=\text{N}^+\text{H}$ ) in the



**Table 7** The main core lines found in API 5L X70 C-steel samples in 3.5% NaCl solution have binding energies (eV) and their assignments associated with  $1.0 \times 10^{-4}$  M of  $\text{H}_2\text{TTAH}$  and  $\text{Zn-H}_2\text{TTAH}$  complex at  $25 \pm 1$  °C

API 5L X70 C-steel in 3.5% NaCl solution treated with $1.0 \times 10^{-4}$ M of $\text{H}_2\text{TTAH}$			API 5L X70 C-steel in 3.5% NaCl solution treated with $1.0 \times 10^{-4}$ M of $\text{Zn-H}_2\text{TTAH}$		
Core element	BE, eV	Assignments	Core element	BE, eV	Assignments
C 1s	285.08	–C–H, –C–C–, –C=C–	C 1s	285.01	–C–H, –C–C–, –C=C–
	286.74	–C–N, –C–Cl		285.57	–C–N, –C–Cl
	288.51	–C–N <sup>+</sup>		288.67	–C–N <sup>+</sup>
Cl 2p	198.41	Cl 2p <sub>3/2</sub>	Cl 2p	199.66	Cl 2p <sub>3/2</sub>
	200.47	Cl 2p <sub>1/2</sub>		200.98	Cl 2p <sub>1/2</sub>
Fe 2p	710.97	Fe 2p <sub>3/2</sub> of Fe <sup>2+</sup>	Fe 2p	710.73	Fe 2p <sub>3/2</sub> of Fe <sup>2+</sup>
	713.40	Fe 2p <sub>3/2</sub> of Fe <sup>3+</sup>		712.54	Fe 2p <sub>3/2</sub> of Fe <sup>3+</sup>
	717.23	Satellite Fe 2p <sub>3/2</sub> of Fe <sup>2+</sup>		716.02	Satellite Fe 2p <sub>3/2</sub> of Fe <sup>2+</sup>
	720.28	Satellite Fe 2p <sub>3/2</sub> of Fe <sup>3+</sup>		719.75	Satellite Fe 2p <sub>3/2</sub> of Fe <sup>3+</sup>
	724.62	Fe 2p <sub>1/2</sub> of Fe <sup>2+</sup>		724.56	Fe 2p <sub>1/2</sub> of Fe <sup>2+</sup>
	728.06	Fe 2p <sub>1/2</sub> of Fe <sup>3+</sup>		727.82	Fe 2p <sub>1/2</sub> of Fe <sup>3+</sup>
	733.11	Satellite Fe 2p <sub>1/2</sub> of Fe <sup>3+</sup>		732.94	Satellite Fe 2p <sub>1/2</sub> of Fe <sup>3+</sup>
O 1s	530.03	FeO, Fe <sub>2</sub> O <sub>3</sub>	O 1s	530.02	FeO, Fe <sub>2</sub> O <sub>3</sub>
	531.26	FeOOH		531.63	FeOOH
N 1s	399.95	–C=N–, N–Fe	N 1s	399.68	–C=N–, N–Fe
	402.23	–C=N <sup>+</sup> –		400.63	–C=N <sup>+</sup> –
S 2p	163.43	S 2p <sub>3/2</sub> of S in thiophene, S–Fe	S 2p	161.73	S 2p <sub>3/2</sub> of S in thiophene
	165.36	S 2p <sub>3/2</sub> of S in thiophene		163.70	S 2p <sub>3/2</sub> of S in thiophene, S–Fe
	167.86	S 2p <sub>1/2</sub> of S in thiophene		166.83	S 2p <sub>1/2</sub> of S in thiophene
	169.67	Fe–S		168.41	Fe–S
			Zn 2p	1022.64	Zn 2p <sub>3/2</sub> of Zn <sup>2+</sup>
				1045.02	Zn 2p <sub>1/2</sub> of Zn <sup>2+</sup>

$\text{H}_2\text{TTAH}$  and  $\text{Zn-H}_2\text{TTAH}$  inhibitors.<sup>66</sup> Furthermore, the S 2p spectra show distinct peaks (Fig. 7 and 8). Peaks at energies of 161.73, 163.43, 163.70, and 165.36 eV are associated with neutral sulfur in the thiophen ring. Peaks at energies of 167.86 and 166.83 eV are attributed to neutral sulfur in the thiophen ring,<sup>67,68</sup> while peaks at energies of 168.41 and 169.67 eV indicate the formation of S–Fe bond.<sup>54,69</sup> Additionally, the Zn 2p XPS spectra of the specimen treated with the  $\text{Zn-H}_2\text{TTAH}$  complex exhibit two characteristic peaks (Fig. 8): one at 1022 eV for Zn 2p<sub>3/2</sub> of Zn<sup>2+</sup> and another at 1045.02 eV for Zn 2p<sub>1/2</sub> of Zn<sup>2+</sup>, confirming the adsorption of the  $\text{Zn-H}_2\text{TTAH}$  complex on the surface of the API 5L X70 C-steel.<sup>70</sup> These findings obtained from XPS analysis support the adsorption of the  $\text{H}_2\text{TTAH}$  and  $\text{Zn-H}_2\text{TTAH}$  compounds on the API 5L X70 C-steel surface in 3.5% NaCl solution.

### 3.6. DFT studies

Fig. 9 illustrates the optimized structures, LUMO, and HOMO distribution of  $\text{H}_2\text{TTAH}$  and  $\text{Zn-H}_2\text{TTAH}$  molecules. The equivalent theoretical variables are provided in Table 8. In accordance with the FMO theory, the LUMO and HOMO energies indicate the inhibitor molecule ability for electrons contribution or acceptance with the surface of the metal.<sup>56</sup> So, an inhibitor particle with a high  $E_{\text{HOMO}}$  and low  $E_{\text{LUMO}}$  values demonstrates superior corrosion protection properties. Created on the data in Table 8, the  $\text{Zn-H}_2\text{TTAH}$  molecule displays the highest  $E_{\text{HOMO}}$  value (–5.05 eV) compared to the  $\text{H}_2\text{TTAH}$  molecule (–5.14 eV) implies better protective power for  $\text{Zn-H}_2\text{TTAH}$  molecule. According to Fig. 9, the HOMO level of the inhibitor particles primarily resides in the thiophen and

acetohydrazide moieties, representing that these regions are extra disposed to electrophilic attacks on the X70-Steel surface. These findings provide the inhibitor ability to adsorb onto the steel surface, thereby enhancing its protective efficiency, which aligns with the experimental results. However, it should be noted that the  $E_{\text{LUMO}}$  value for the  $\text{Zn-H}_2\text{TTAH}$  molecule (–2.74 eV) is inferior to that of the  $\text{H}_2\text{TTAH}$  molecule (–2.43 eV). Consistent with previous observations, this lower  $E_{\text{LUMO}}$  value for the  $\text{Zn-H}_2\text{TTAH}$  molecule signifies its greater protective power.

Similarly, it is crucial to decrease the energy gap ( $\Delta E$ ) value so as to enhance the effectiveness of the corrosion inhibitor additive.<sup>57</sup> As disclosed in Table 8, the  $\text{Zn-H}_2\text{TTAH}$  molecule has a higher probability of being adsorbed at the interface of X70-Steel, as indicated by its lower  $\Delta E$  value of 2.31 eV compared to the  $\text{H}_2\text{TTAH}$  molecule with a  $\Delta E$  value of 2.71 eV. Generally, inhibitors exhibit moderately low electronegativity values ( $\chi$ ), demonstrating their competence to contribute electrons to the steel surface.<sup>58</sup> Conversely, a high electronegativity ( $\chi$ ) of the inhibitor particle enables it to efficiently receive electrons from the atoms at the steel interface followed by back donation from inhibitor particles and usage of a stronger bond with the steel surface.<sup>71</sup> According to the data in Table 8, both the  $\text{H}_2\text{TTAH}$  and  $\text{Zn-H}_2\text{TTAH}$  molecules have slightly higher electronegativity values, which allows for effective electron acceptance from the steel interface trucked by back donation to the metal surface, leading to a robust connection with the steel surface. Moreover, the molecule's softness ( $\sigma$ ) and hardness ( $\eta$ ) can be employed to assess its reactivity and stability. Soft molecules characterized by a seamless electron transfer to the steel





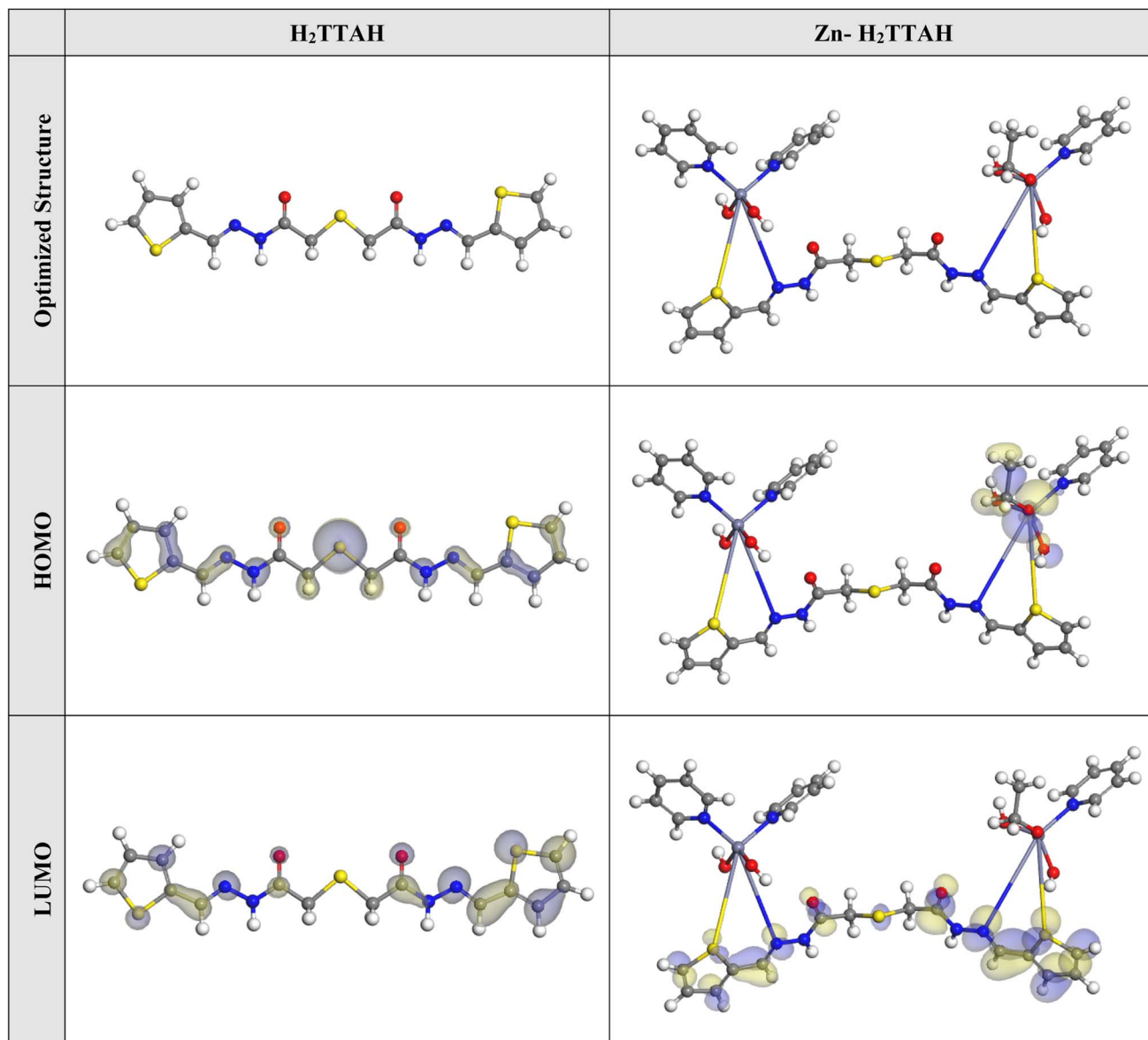


Fig. 9 The optimized molecular structures, HOMO and LUMO of the H<sub>2</sub>TTAH and Zn-H<sub>2</sub>TTAH using DMol<sup>3</sup> module.

Table 8 The computed DFT quantum chemical variables for H<sub>2</sub>TTAH and Zn-H<sub>2</sub>TTAH compounds

Parameters	H <sub>2</sub> TTAH	Zn-H <sub>2</sub> TTAH
$E_{\text{HOMO}}$ (eV)	−5.14	−5.05
$E_{\text{LUMO}}$ (eV)	−2.43	−2.74
$\Delta E = E_{\text{LUMO}} - E_{\text{HOMO}}$ (eV)	2.71	2.31
Electronegativity ( $\chi$ )	3.79	3.89
Global hardness ( $\eta$ )	1.35	1.15
Global softness ( $\sigma$ )	0.74	0.87
The number of electrons transferred ( $\Delta N$ )	1.19	1.35
$\Delta E_{\text{back-donation}}$	−0.34	−0.29
Dipole moments ( $\mu$ ) debye	14.99	18.80
Molecular surface area, Å <sup>2</sup>	385.00	809.78

interface during adsorption, exhibit superior corrosion protection capabilities compared to hard molecules. Hence, these molecules act as effective corrosion inhibitors.<sup>72</sup> Table 8 demonstrates that the Zn-H<sub>2</sub>TTAH molecule displays higher  $\sigma$  values and smaller  $\eta$  values than the H<sub>2</sub>TTAH particle. This indicates a more efficient electron transfer to the metal substrate and superior inhibition possessions for Zn-H<sub>2</sub>TTAH molecule.

Furthermore, the part of electron transfer and the  $\Delta E_{\text{back-donation}}$  are important variables in determining the inhibitor's capability to provide or receive electrons. If  $\Delta N$  values are greater than 0, it suggests that electron transfer occurs from the inhibitor to the metal interface. While, if  $\Delta N$  values are less than or equal to zero, it becomes possible for electron transfer from the metal to the inhibitor molecule (*i.e.*, back donation).<sup>61,73</sup> By examining the recorded  $\Delta N$  values in Table 8, it can be noticed



that the molecules **Zn-H<sub>2</sub>TTAH** and **H<sub>2</sub>TTAH** have positive  $\Delta N$  values, indicating their capacity to provide electrons to the surface of metal. Moreover, when  $\eta > 0$ , the  $\Delta E_{\text{back-donation}}$  value becomes  $< 0$ , implying the relocate of electrons from the metal to the molecule and their subsequent donation back to the molecule, which is a desired dynamic process.<sup>74</sup> Table 8 shows negative values of  $\Delta E_{\text{back-donation}}$  for the **Zn-H<sub>2</sub>TTAH** and **H<sub>2</sub>TTAH** molecules, suggesting a preference for back donation in these particles and the creation of a strong bond.<sup>62</sup>

Moreover, the dipole moment is a critical parameter that significantly influences the corrosion inhibition efficacy.<sup>75</sup> An improvement in the dipole moment raises the energy required for distortion and expands the examined particle adsorption on the metal surface. Hence, a greater dipole moment contributes to a greater inhibiting proficiency.<sup>76</sup> As outlined in Table 8, the **Zn-H<sub>2</sub>TTAH** compound possesses a larger dipole moment value (18.80 debye) in comparison to the **H<sub>2</sub>TTAH** molecule (14.99 debye), indicating a higher tendency for adsorption on the steel interface and an enhanced prohibition capability. Additionally, there exists a clear association between the surface area of molecules of the **Zn-H<sub>2</sub>TTAH** and **H<sub>2</sub>TTAH** molecules and their ability to protect the X-70 surface in destructive media. A larger molecular structure leads to higher inhibition proficiency as it increases the interface area between the inhibitor particles and the examined surface. Henceforth, the **Zn-H<sub>2</sub>TTAH** molecule demonstrates the larger molecular surface area (809.78 Å<sup>2</sup>) than **H<sub>2</sub>TTAH** molecule (385.00 Å<sup>2</sup>), owing to the existence of three extra pyridine rings in the **Zn-H<sub>2</sub>TTAH** structure in comparison

with **H<sub>2</sub>TTAH** structure, and consequently exhibits an increased rate of inhibition in comparison to the **H<sub>2</sub>TTAH** particles, as displayed in Table 8.

In addition, the Dmol<sup>3</sup> module was applied to evaluate the active sites of the examined compounds species by means of molecular electrostatic potential mapping (MEP). MEP is a visual representation in three dimensions that aims to identify the overall electrostatic influence exerted on a compound by its charge distribution.<sup>67</sup> The MEP illustrated in Fig. 10 display regions of intense electron density in red, indicating a strongly negative MEP (associated with nucleophilic reactions). Conversely, the blue regions represent the highest positive areas (related to electrophilic interactions).<sup>35</sup> Analysis of Fig. 10 reveals that the areas with the most negative values are primarily situated above the thiophen moieties and pyridine rings, while the acetohydrazide moieties have lower electron density. These regions with greater electron density (indicated by the red area) in the investigated compounds are likely the greatest favorable for interactions with the steel interface, configuring of durable adsorbed protecting layers.

### 3.7. MC simulations

The Monte Carlo simulations were conducted to gain insights into the interactions between the inhibitor particles and the investigated metal. This was done to propose a plausible adsorption mechanism. Fig. 11 demonstrates that the **Zn-H<sub>2</sub>TTAH** and **H<sub>2</sub>TTAH** molecules exhibited the most favorable adsorption configurations at the interface of the X70 Steel in the

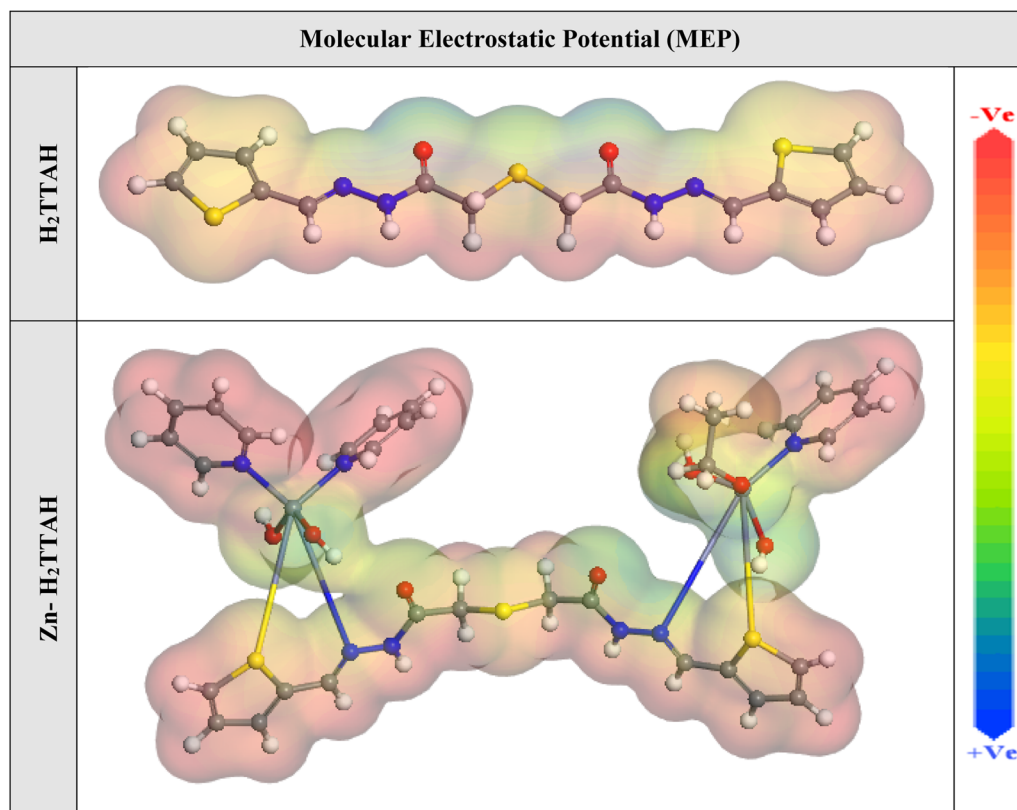


Fig. 10 The graphical representation of the MEP for the **H<sub>2</sub>TTAH** and **Zn-H<sub>2</sub>TTAH** was conducted utilizing the Dmol<sup>3</sup> module.

3.5% NaCl solution. The module used for adsorption configurations indicated that these molecules were adsorbed in a nearly flat orientation, indicating enhanced adsorption and maximum coverage of the surface examined.<sup>77,78</sup>

Additionally, Table 9 presents the adsorption energies attained from Monte Carlo simulations. It was observed that the **Zn-H<sub>2</sub>TTAH** compound ( $-2710.79 \text{ kcal mol}^{-1}$ ) exhibited a more negative adsorption energy value associated to the **H<sub>2</sub>TTAH** compound ( $-2469.46 \text{ kcal mol}^{-1}$ ), representing a stronger adsorption of the **Zn-H<sub>2</sub>TTAH** on the steel surface. This suggests

that the **Zn-H<sub>2</sub>TTAH** compound forms a stable adsorbed film, providing effective corrosion inhibition for the steel, which aligns with the experimental findings.<sup>78,79</sup> Furthermore, Table 9 also exhibits that the adsorption energy value for the **Zn-H<sub>2</sub>TTAH** compound in the unrelaxed state ( $-2968.82 \text{ kcal mol}^{-1}$ ) is more negative compared to the **H<sub>2</sub>TTAH** molecule ( $-2469.46 \text{ kcal mol}^{-1}$ ). Similarly, in the relaxed state after geometry optimization, the adsorption energy values for the **Zn-H<sub>2</sub>TTAH** compound ( $258.03 \text{ kcal mol}^{-1}$ ) are more than those of the **H<sub>2</sub>TTAH** compound

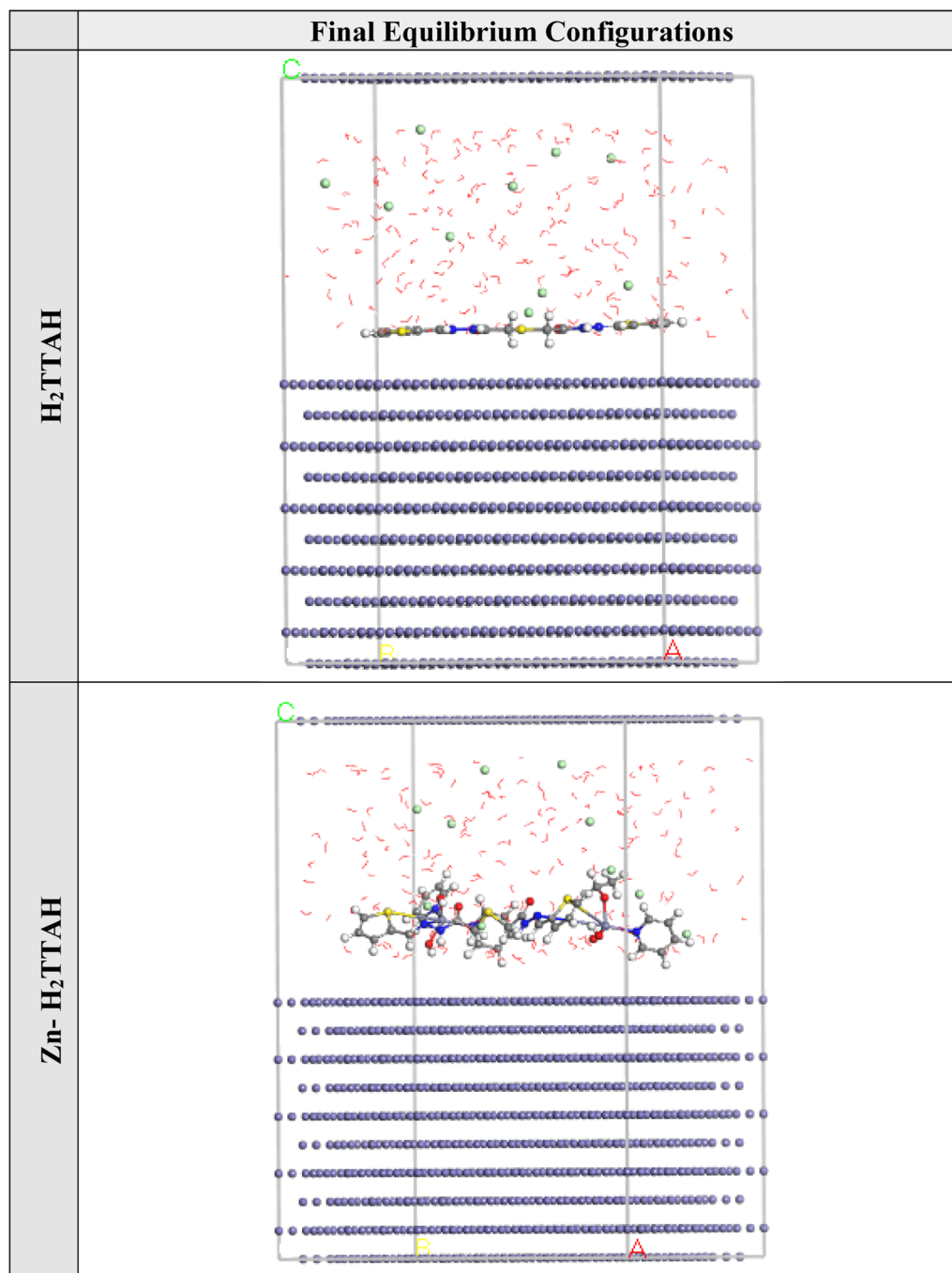


Fig. 11 The optimal arrangement of the adsorption for the **H<sub>2</sub>TTAH** and **Zn-H<sub>2</sub>TTAH** on the Fe (1 1 0) substrate was computed utilizing the adsorption locator module.



**Table 9** Data derived from the application the Mont Carlo simulation (MC) for adsorption of the  $\text{H}_2\text{TTAH}$  and  $\text{Zn-H}_2\text{TTAH}$  compounds on Fe (1 1 0)

Corrosion systems	Adsorption energy (kcal mol <sup>-1</sup> )	Rigid adsorption energy (kcal mol <sup>-1</sup> )	Deformation energy (kcal mol <sup>-1</sup> )	$dE_{\text{ads}}/dN_i$ : inhibitor (kcal mol <sup>-1</sup> )	$dE_{\text{ads}}/dN_i$ : Cl <sup>-</sup> ions (kcal mol <sup>-1</sup> )	$dE_{\text{ads}}/dN_i$ : water (kcal mol <sup>-1</sup> )
Fe (1 1 0) <b>H<sub>2</sub>TTAH</b> Water Cl <sup>-</sup> ions	-2469.46	-2469.46	208.26	-244.02	-101.24	-18.17
Fe (1 1 0) <b>Zn-H<sub>2</sub>TTAH</b> Water Cl <sup>-</sup> ions	-2710.79	-2968.82	258.03	-294.55	-102.67	-18.50

(208.26 kcal mol<sup>-1</sup>). This confirms the higher corrosion prohibition of the **Zn-H<sub>2</sub>TTAH** compound compared to the **H<sub>2</sub>TTAH**.

The  $dE_{\text{ads}}/dN_i$  values afford information about the energy of the arrangement between the investigated metal and the adsorbates, specifically when excluding the adsorbed inhibitor compound or other adsorbates compounds.<sup>71</sup> Table 9 shows that the  $dE_{\text{ads}}/dN_i$  values of **Zn-H<sub>2</sub>TTAH** molecules (-294.55 kcal mol<sup>-1</sup>) are greater than that of the **H<sub>2</sub>TTAH** compound (-244.02 kcal mol<sup>-1</sup>), indicating that the **Zn-H<sub>2</sub>TTAH** molecule has stronger adsorption than the **H<sub>2</sub>TTAH** molecule. The  $dE_{\text{ads}}/dN_i$  values for water particles and chloride ions are approximately -18.36 and -101.96 kcal mol<sup>-1</sup>, correspondingly. These values imply that the adsorption of the inhibitor compounds is stronger than that of water particles and chloride ions, leading to the substitution of water particles and chloride ions by the inhibitor compounds.<sup>80</sup> Therefore, the **Zn-H<sub>2</sub>TTAH** molecule forms a firmly attached protecting film on the steel surface, resulting in effective corrosion inhibition in a corrosive media, as supported by practical and theoretical findings.<sup>81</sup>

### 3.8. The corrosion inhibition mechanism

Neutral corrosive environments are thought to prevent metal corrosion by forming a shielding layer through the adsorption of inhibitor particles on the examined metal.<sup>82</sup> The adsorption process helps preserve the examined metal surface under corrosive conditions. The adsorption of **H<sub>2</sub>TTAH** and **Zn-H<sub>2</sub>TTAH** molecules can be categorized into two different categories of interactions: physisorption and chemisorption.<sup>46</sup> Physisorption occurs when there is a charged surface on the metal and charged particles in the solution. The electric field at the metal/solution interface induces a surface charge on the metal.<sup>83</sup> Conversely, chemisorption contains the relocation of electrons from the inhibitor particles to the metal surface, resulting in the creation of a coordination bond.<sup>84</sup>

Regardless of the charge on the surface, it is possible to achieve inhibition. It is crucial for the inhibitor to consist of molecules that have heteroatoms, or electrons with weak ties with a lone pair of electrons.<sup>42</sup> In addition, a transition metal with low-energy unoccupied electron orbitals, such as Fe<sup>2+</sup> and Fe<sup>3+</sup>, is necessary. Two main categories of inhibition mechanisms have been anticipated. One involves the creation of complexes with iron ions (Fe<sup>2+</sup> and Fe<sup>3+</sup>), depending on the

environment.<sup>24</sup> One more aspect involves the chemical adsorption of **H<sub>2</sub>TTAH** and its Zn complex onto steel surfaces. This occurs by way of the development of coordinate linkages between the active sites of **H<sub>2</sub>TTAH** and its Zn complex (specifically, nitrogen atoms with lone pairs of electrons and benzene rings with  $\pi$ -electrons) and the vacant d-orbitals of the iron surface. Chemical adsorption is indicated by the values of  $\Delta G_{\text{ads}}^{\circ}$  (>40 kJ mol<sup>-1</sup>), which suggests that **H<sub>2</sub>TTAH** and its Zn complex are chemically adsorbed on the steel surface.

The corrosion inhibition effectiveness of **Zn-H<sub>2</sub>TTAH** is higher than that of **H<sub>2</sub>TTAH**. This is attributed to the larger pyridine group in **Zn-H<sub>2</sub>TTAH**, which provides more sites for electrophilic attack. Moreover, **Zn-H<sub>2</sub>TTAH** has a lower  $E_{\text{HOMO}}$ , lower  $\Delta E$ , and lower hardness, which all contribute to its strong inhibitory efficiency. The confirmation of chemical adsorption is based on the interface between the inhibitor molecules and the vacant d-orbital of the iron atom. This interaction involves electron transfer, electron sharing, and the construction of covalent (co-ordinate), the metal surface and the inhibitor particles are connected by bonds.<sup>85</sup>



By examining eqn (13) and (14), several observations can be made:<sup>86,87</sup> (i) the corrosion products are generated at an enhanced rate because of carbon steel dissolution in the anode region, (ii) the cathode region experiences oxygen reduction reaction, subsequent in the establishment of OH<sup>-</sup> ions, and (iii) a variety of Fe<sup>2+</sup> and Fe<sup>3+</sup> compounds, such as FeCl<sub>3</sub>, iron hydroxide (Fe(OH)<sub>2</sub>, Fe(OH)<sub>3</sub>), and iron oxides (Fe<sub>3</sub>O<sub>4</sub>,  $\gamma$ -Fe<sub>2</sub>O<sub>3</sub>), form on the steel surface.

## 4. Conclusion

(1) The **H<sub>2</sub>TTAH** and **Zn-H<sub>2</sub>TTAH** exhibited impressive inhibition properties against API 5L X70 carbon steel corrosion in 3.5% NaCl solutions reached 93.4%, 96.1% and serving as efficacious suppressants for both anodic and cathodic processes.

(2) The electrochemical measurements (PP and EIS) clearly indicate that the inhibition efficiency expands with raising the





inhibitor concentrations. The order of efficiency for inhibition is as follows: **Zn-H<sub>2</sub>TTAH** > **H<sub>2</sub>TTAH**.

(3) The corrosion inhibition behavior of these compounds within a corrosive media is demonstrated by the pronounced increase in  $R_{ct}$  values, coupled with the simultaneous decrease in  $CPE_{dl}$  values, upon the introduction of  $1 \times 10^{-4}$  M concentrations of the **H<sub>2</sub>TTAH** and **Zn-H<sub>2</sub>TTAH**.

(4) The adsorption of the **H<sub>2</sub>TTAH** and **Zn-H<sub>2</sub>TTAH** molecules on the API 5L X70 carbon steel surface in 3.5% NaCl solutions conforms to the Langmuir adsorption isotherm.

(5) The adsorption of the **H<sub>2</sub>TTAH** and **Zn-H<sub>2</sub>TTAH** inhibitors is spontaneous process, as implied by the significant negative value of  $\Delta G_{ads}^\circ$ .

(6) XPS was utilized to confirm the adsorption of **H<sub>2</sub>TTAH** and **Zn-H<sub>2</sub>TTAH** molecules on the API 5L X70 carbon steel surface which matching with corrosion mechanism.

(7) The data obtained from PP and EIS techniques confirmed the effectiveness of the **H<sub>2</sub>TTAH** and **Zn-H<sub>2</sub>TTAH** molecules as corrosion inhibitors. Furthermore, a significant congruence was observed between the empirical findings and theoretical predictions.

## Author contributions

Ola. A. El-Gammal: conceptualization, supervision, investigation, methodology, resources, formal analysis, data curation, funding acquisition, writing – original draft, writing – review & editing. Dena A. Saad: conceptualization, supervision, investigation, methodology, resources, formal analysis, data curation, funding acquisition, writing – original draft, writing – review & editing. Marwa N. El-Nahass: conceptualization, supervision, investigation, methodology, resources, formal analysis, data curation, funding acquisition, writing – original draft, writing – review & editing. Kamal Shalabi: conceptualization, supervision, investigation, methodology, resources, formal analysis, data curation, funding acquisition, writing – original draft, writing – review & editing. Yasser M. Abdallah: conceptualization, supervision, investigation, methodology, resources, formal analysis, data curation, funding acquisition, writing – original draft, writing – review & editing.

## Conflicts of interest

The authors declare that they have no known competing financial interests or personal relationships that could have appeared to influence the work reported in this paper.

## References

- 1 A. Y. Yassin, A. M. Abdelghany, M. M. Shaban and Y. M. Abdallah, *Colloids Surf., A*, 2022, **635**, 128115.
- 2 Y. M. Abdallah, O. A. El-Gammal, H. M. Abd El-Lateef and K. Shalabi, *RSC Adv.*, 2022, **12**, 14665–14685.
- 3 O. M. A. Khamaysa, I. Selatnia, H. Zeghache, H. Lgaz, A. Sid, I.-M. Chung, M. Benahmed, N. Gherraf and P. Mosset, *J. Mol. Liq.*, 2020, **315**, 113805.
- 4 L. Boucherit, T. Douadi, N. Chafai, M. Al-Noaimi and S. Chafaa, *Int. J. Electrochem. Sci.*, 2018, **13**, 3997–4025.
- 5 L. Herrag, B. Hammouti, S. Elkadiri, A. Aouniti, C. Jama, H. Vezin and F. Bentiss, *Corros. Sci.*, 2010, **52**, 3042–3051.
- 6 A. Zeino, I. Abdulazeez, M. Khaled, M. W. Jawich and I. B. Obot, *J. Mol. Liq.*, 2018, **250**, 50–62.
- 7 Y.-C. Dai, W. Yang, X. Chen, L.-H. Gao and K.-Z. Wang, *Electrochim. Acta*, 2014, **134**, 319–326.
- 8 L. Yang, X. Li, Y. Xiong, X. Liu, X. Li, M. Wang, S. Yan, L. A. M. Alshahrani, P. Liu and C. Zhang, *J. Electroanal. Chem.*, 2014, **731**, 14–19.
- 9 X. Li, Y. Li, R. Feng, D. Wu, Y. Zhang, H. Li, B. Du and Q. Wei, *Sens. Actuators, B*, 2013, **188**, 462–468.
- 10 H. M. Abd El-Lateef, A. R. Sayed and M. S. S. Adam, *Appl. Organomet. Chem.*, 2019, **33**, e4987.
- 11 A. a. A. Massoud, A. Hefnawy, V. Langer, M. A. Khatib, L. Öhrstrom and M. A. M. Abu-Youssef, *Polyhedron*, 2009, **28**, 2794–2802.
- 12 S. R. Gupta, P. Mourya, M. M. Singh and V. P. Singh, *J. Mol. Struct.*, 2017, **1137**, 240–252.
- 13 M. Mishra, K. Tiwari, A. K. Singh and V. P. Singh, *Polyhedron*, 2014, **77**, 57–65.
- 14 A. M. Abdel-Gaber, M. S. Masoud, E. A. Khalil and E. E. Shehata, *Corros. Sci.*, 2009, **51**, 3021–3024.
- 15 M. Mahdavian and R. Naderi, *Corros. Sci.*, 2011, **53**, 1194–1200.
- 16 M. Mahdavian and M. M. Attar, *Corros. Sci.*, 2009, **51**, 409–414.
- 17 S. J. Rowan, S. J. Cantrill, G. R. L. Cousins, J. K. M. Sanders and J. F. Stoddart, *Angew. Chem.*, 2002, **114**, 938–993.
- 18 J. V. Ragavendran, D. Sriram, S. K. Patel, I. V. Reddy, N. Bharathwajan, J. Stables and P. Yogeeswari, *Eur. J. Med. Chem.*, 2007, **42**, 146–151.
- 19 K. B. Gudasi, S. A. Patil, R. S. Vadavi, R. V. Shenoy and M. S. Patil, *Transition Met. Chem.*, 2005, **30**, 726–732.
- 20 S. K. Ahmed, W. B. Ali and A. A. Khadom, *Int. J. Ind. Chem.*, 2019, **10**, 159–173.
- 21 H. Lgaz, A. Chaoui, M. R. M. R. Albayati, R. Salghi, Y. El Aoufir, I. H. I. H. Ali, M. I. M. I. Khan, S. K. S. K. Mohamed and I.-M. I. M. Chung, *Res. Chem. Intermed.*, 2019, **45**, 2269–2286.
- 22 N. Chafai, S. Chafaa, K. Benbouguerra, A. Hellal and M. Mehri, *J. Mol. Struct.*, 2019, **1181**, 83–92.
- 23 H. Lgaz, I.-M. Chung, M. R. Albayati, A. Chaoui, R. Salghi and S. K. Mohamed, *Arabian J. Chem.*, 2020, **13**, 2934–2954.
- 24 N. Aissiou, M. Bounoughaz and A. Djeddi, *Chem. Res. Chin. Univ.*, 2021, **37**, 718–728.
- 25 H. M. A. El-Lateef, K. A. Soliman, M. A. Al-Omar and M. S. S. Adam, *J. Taiwan Inst. Chem. Eng.*, 2021, **120**, 391–408.
- 26 M. Chafiq, A. Chaoui, M. R. Al-Hadeethi, R. Salghi, A. H. Ismat, M. K. Shaaban and I. M. Chung, *Colloids Surf., A*, 2021, **610**, 125744.
- 27 H. Zimmer and E. Shaheen, *J. Org. Chem.*, 1959, **24**, 1140–1141.
- 28 H. M. Abd El-Lateef, M. M. Khalaf, M. Gouda, K. Shalabi, F. El-Taib Heikal, A. S. M. Al-Janabi and S. Shaaban, *Constr. Build. Mater.*, 2023, **366**, 130135.



- 29 H. M. A. El-Lateef, Z. A. Abdallah and M. S. M. Ahmed, *J. Mol. Liq.*, 2019, **296**, 111800.
- 30 H. M. Abd El-Lateef, M. M. Khalaf, K. Shalabi and A. A. Abdelhamid, *Chin. J. Chem. Eng.*, 2023, **55**, 304–319.
- 31 O. A. El-Gammal, D. A. Saad and A. F. Al-Hossainy, *J. Mol. Struct.*, 2021, **1244**, 130974.
- 32 O. A. El-Gammal, E. A. Elmorsy and Y. E. Sherif, *Spectrochim. Acta, Part A*, 2014, **120**, 332–339.
- 33 O. A. El-Gammal, M. M. Bekheit and M. Tahoon, *Spectrochim. Acta, Part A*, 2015, **135**, 597–607.
- 34 Q. H. Zhang, B. S. Hou and G. A. Zhang, *J. Colloid Interface Sci.*, 2020, **572**, 91–106.
- 35 H. M. Al-Saidi, G. A. Gouda, M. Abdel-Hakim, N. I. Alsenani, A. Alfarsi, M. H. Mahross, O. A. Farghaly and S. Hosny, *Int. J. Electrochem. Sci.*, 2022, **17**, 220333.
- 36 R. N. El-Tabesh, A. M. Abdel-Gaber, H. H. Hammud and R. Oweini, *J. Bio- Tribo-Corros.*, 2020, **6**, 46.
- 37 H. M. Abd El-Lateef, K. Shalabi, A. M. Arab and Y. M. Abdallah, *ACS Omega*, 2022, **7**, 23380–23392.
- 38 M. M. Solomon, S. A. Umoren, M. A. Quraishi and M. Salman, *J. Colloid Interface Sci.*, 2019, **551**, 47–60.
- 39 F. Rosalbino, G. Scavino, G. Mortarino, E. Angelini and G. Lunazzi, *J. Solid State Electrochem.*, 2010, **15**, 703–709.
- 40 E. A. Noor, *Mater. Chem. Phys.*, 2009, **114**, 533–541.
- 41 M. S. Shaaban, K. Shalabi, A. E. A. S. Fouda and M. A. Deyab, *Z. fur Phys. Chem.*, 2023, **237**, 211–241.
- 42 M. Ontiveros-Rosales, A. Espinoza-Vázquez, F. J. Rodríguez Gómez, S. Valdez-Rodríguez, A. Miralrio, B. A. Acosta-Garcia and M. Castro, *J. Mol. Liq.*, 2022, **363**, 119826.
- 43 A. Salhi, A. Elyoussfi, I. Azghay, A. El Aatiaoui, H. Amhamdi, M. El Massaoudi, M. h. Ahari, A. Bouyanzer, S. Radi and S. El barkany, *Inorg. Chem. Commun.*, 2023, **152**, 110684.
- 44 M. Hosseini, S. F. L. Mertens, M. Ghorbani and M. R. Arshadi, *Mater. Chem. Phys.*, 2003, **78**, 800–808.
- 45 K. M. Abd El-Khalek, K. Shalabi, M. A. Ismail and A. E.-A. S. Fouda, *RSC Adv.*, 2022, **12**, 10443–10459.
- 46 M. En-Nilly, S. Skal, Y. El aoufir, H. Lgaz, R. J. Adnin, A. A. Alrashdi, A. Bellaouchou, M. R. Al-Hadeethi, O. Benali, T. Guedira, H. S. Lee, S. Kaya and S. M. Ibrahim, *Arabian J. Chem.*, 2023, **16**, 104711.
- 47 A. G. Sayed, A. M. Ashmawy, W. E. Elgammal, S. M. Hassan and M. A. Deyab, *Sci. Rep.*, 2023, **13**, 13761.
- 48 A. R. Sayed and H. M. A. El-Lateef, *Coatings*, 2020, **10**, 1068.
- 49 M. Chafiq, A. Chaouiki, M. R. Al-Hadeethi, I. H. Ali, S. K. Mohamed, K. Toumiat and R. Salghi, *Coatings*, 2020, **10**, 700.
- 50 S. S. Alarfaji, I. H. Ali, M. Z. Bani-Fwaz and M. A. Bedair, *Molecules*, 2021, **26**, 3183.
- 51 H. Keleş, D. M. Emir and M. Keleş, *Corros. Sci.*, 2015, **101**, 19–31.
- 52 M. Das, A. Biswas, B. Kumar Kundu, M. Adilia Januário Charmier, A. Mukherjee, S. M. Mobin, G. Udayabhanu and S. Mukhopadhyay, *Chem. Eng. J.*, 2019, **357**, 447–457.
- 53 K. Subbiah, H.-S. Lee, M. R. Al-Hadeethi, T. Park and H. Lgaz, *J. Adv. Res.*, 2023, **58**, 211–228.
- 54 A. K. Singh, S. Thakur, B. Pani, B. Chugh, H. Lgaz, I.-M. Chung, P. Chaubey, A. K. Pandey and J. Singh, *J. Mol. Liq.*, 2019, **283**, 788–803.
- 55 G. Pandimuthu, K. Muthupandi, T.-W. Chen, S.-M. Chen, A. Sankar, P. Muthukrishnan and S.-P. Rwei, *Int. J. Electrochem. Sci.*, 2021, **16**, 211153.
- 56 H. Ouici, M. Tourabi, O. Benali, C. Selles, C. Jama, A. Zarrouk and F. Bentiss, *J. Electroanal. Chem.*, 2017, **803**, 125–134.
- 57 G. Fan, H. Liu, B. Fan, Y. Ma, H. Hao and B. Yang, *J. Mol. Liq.*, 2020, **311**, 113302.
- 58 M. Bouanis, M. Tourabi, A. Nyassi, A. Zarrouk, C. Jama and F. Bentiss, *Appl. Surf. Sci.*, 2016, **389**, 952–966.
- 59 A. Berrissoul, A. Ouarrach, F. Benhiba, A. Romane, A. Guenbour, B. Dikici, F. Bentiss, A. Zarrouk and A. Dafali, *Ind. Crops Prod.*, 2022, **187**, 115310.
- 60 N. Z. N. Hashim, E. H. Anouar, K. Kassim, H. M. Zaki, A. I. Alharthi and Z. Embong, *Appl. Surf. Sci.*, 2019, **476**, 861–877.
- 61 P. Bommersbach, C. Alemany-Dumont, J. P. Millet and B. Normand, *Electrochim. Acta*, 2005, **51**, 1076–1084.
- 62 W. Temesghen and P. Sherwood, *Anal. Bioanal. Chem.*, 2002, **373**, 601–608.
- 63 A. Zarrouk, B. Hammouti, T. Lakhli, M. Traisnel, H. Vezin and F. Bentiss, *Corros. Sci.*, 2015, **90**, 572–584.
- 64 P. Mourya, P. Singh, R. B. Rastogi and M. M. Singh, *Appl. Surf. Sci.*, 2016, **380**, 141–150.
- 65 V. M. Paiva, R. d. S. Nunes, K. C. d. S. de Lima, S. M. de Oliveira, J. R. de Araujo, B. S. Archanjo, A. F. do Valle and E. D'Elia, *Surf. Interfaces*, 2024, **47**, 104187.
- 66 K. Shalabi, H. M. Abd El-Lateef, M. M. Hammouda, A. M. A. Osman, A. H. Tantawy and M. A. Abo-Riya, *Materials*, 2023, **16**, 5192.
- 67 Y. Kharbach, F. Z. Qachchachi, A. Haoudi, M. Tourabi, A. Zarrouk, C. Jama, L. O. Olasunkanmi, E. E. Ebenso and F. Bentiss, *J. Mol. Liq.*, 2017, **246**, 302–316.
- 68 M. Tourabi, K. Nohair, M. Traisnel, C. Jama and F. Bentiss, *Corros. Sci.*, 2013, **75**, 123–133.
- 69 A. K. Singh, M. Singh, S. Thakur, B. Pani, S. Kaya, B. E. L. Ibrahim and R. Marzouki, *Surf. Interfaces*, 2022, **33**, 102169.
- 70 M. Claros, M. Setka, Y. P. Jimenez and S. Vallejos, *Nanomaterials*, 2020, **10**, 471.
- 71 S. Öztürk, H. Gerengi, M. M. Solomon, G. Gece, A. Yıldırım and M. Yıldız, *Mater. Today Commun.*, 2021, **29**, 102905.
- 72 X. Yang, G. He, W. Dong, L. Yu and X. Li, *J. Environ. Chem. Eng.*, 2023, **11**, 109846.
- 73 I. Lukovits, E. Kálmán and F. Zucchi, *CORROSION*, 2001, **57**, 3–8.
- 74 S. Bousba, H. Allal, M. Damous and S. Maza, *Comput. Theor. Chem.*, 2023, **1225**, 114168.
- 75 S. S. Al-Najjar and A. Y. Al-Baitai, *Phys. Chem. Res.*, 2022, **10**, 179–194.
- 76 H. M. Abd El-Lateef, M. Gouda, M. M. Khalaf, M. A. A. Al-Shuaibi, I. M. A. Mohamed, K. Shalabi and R. M. El-Shishtawy, *Polymers*, 2022, **14**, 3078.
- 77 B. J. Usman, S. A. Umoren and Z. M. Gasem, *J. Mol. Liq.*, 2017, **237**, 146–156.



- 78 H. M. Abd El-Lateef, K. Shalabi and A. H. Tantawy, *J. Mol. Liq.*, 2020, **320**, 114564.
- 79 M. Goyal, H. Vashist, S. Kumar, I. Bahadur, F. Benhiba and A. Zarrouk, *J. Mol. Liq.*, 2020, **315**, 113705.
- 80 L. H. Madkour, S. Kaya and I. B. Obot, *J. Mol. Liq.*, 2018, **260**, 351–374.
- 81 A. Dehghani, A. H. Mostafatabar, G. Bahlakeh and B. Ramezanzadeh, *J. Mol. Liq.*, 2020, **316**, 113914.
- 82 M. Özcan, I. Dehri and M. Erbil, *Appl. Surf. Sci.*, 2004, **236**, 155–164.
- 83 X. Wang, H. Guo, S. Cai and X. Xu, *J. Mol. Struct.*, 2023, **1294**, 136555.
- 84 S. Geng, J. Hu, J. Yu, C. Zhang, H. Wang and X. Zhong, *J. Mol. Struct.*, 2022, **1250**, 131778.
- 85 I. B. Onyeachu and M. M. Solomon, *J. Mol. Liq.*, 2020, **313**, 113536.
- 86 A. M. Al-Sabagh, N. M. Nasser, E. A. Khamis and T. Mahmoud, *Egypt. J. Pet.*, 2017, **26**, 41–51.
- 87 J. Zhang, J. Wang, F. Zhu and M. Du, *Ind. Eng. Chem. Res.*, 2015, **54**, 5197–5203.

